Ocean Engineering 250 (2022) 110874

Contents lists available at ScienceDirect

Ocean Engineering

journal homepage: www.elsevier.com/locate/oceaneng

A semi-analytical one-dimensional model for offshore pile foundations considering effects of pile diameter and aspect ratio

Lilin Wang [a], Takeshi Ishihara [a,*]

[a] Department of Civil Engineering, School of Engineering, The University of Tokyo, 7-3-1, Hongo, Bunkyo-ku, Tokyo, Japan

ARTICLE INFO

Keywords:
Wind turbine
Pile foundations
Semi-analytical 1D model
Pile diameter and aspect ratio
Coupling between axial and lateral resistances
Modal damping

ABSTRACT

A semi-analytical 1D model with the eight types of soil reactions is derived from the fishbone frame model for pile foundations of wind turbines, in which the coupling between axial and lateral resistances that matters for large pile diameters and small pile aspect ratios is modeled as the rotational soil reactions. The only correction factor for the calculation of the ultimate bearing capacities of the lateral and rotational soil reactions on the pile shaft is then identified by a curve-fitting approach and validated using a series of experiments and 3D FE analyses for both sand and clay. The proposed model shows favorable agreements with the experiments and 3D FE analyses in terms of the load-displacement curves at the ground level and the rotation and moment responses for the pile foundations with various pile diameters and aspect ratios. Finally, the proposed model is further verified by monopiles in layered soils and applied to investigate the effect of the coupling between axial and lateral resistances on the modal damping of monopile supported wind turbines. Without considering the coupling between axial and lateral resistances, the modal damping ratios for the monopile supported wind turbine are underestimated significantly.

1. Introduction

In the design of wind turbine supporting structures, it is necessary to consider the fatigue limit state (FLS), serviceability limit state (SLS) and the ultimate limit state (ULS) (DNVGL-ST-0126, 2016). In the dynamic analyses for the FLS and ULS by an aeroelastic model, it is needed to input the accurate modal shapes and modal damping ratios with considering the soil-structure interaction under static and cyclic loadings. As an appealing foundation type of the offshore wind turbine, the monopile foundations with the diameter up to 7.5 m and the aspect ratio of 2–6 have been installed for many years (Kallehave et al., 2015), of which the effects of pile diameter and aspect ratio are believed to be very serious. Widely used in the offshore oil and gas industry, the API p-y curves (API RP 2A-WSD, 2010; API RP 2GEO, 2014) was proposed based on the experimental data of a typical pile diameter of 0.61 m, a penetration length of 21 m, and a large penetration to diameter ratio of 34 (Reese et al., 1974), in which the effects of pile diameter and aspect ratio are not considered since they are not significant for slender piles. In the past decades, the API p-y curves was applied to the design of monopiles since there was not better alternative to consider the soil-monopile interaction. Meantime, many researches (e.g. Shadlou and Bhattacharya, 2016; Yang et al., 2016; Thieken et al., 2015; Achmus et al., 2016; Wang et al., 2020a) pointed out the reliability of API p-y curves is questionable when they are employed for the pile dimensions beyond their originated fields tests. Therefore, two questions arise here. One is how to model the effects of pile diameter and aspect ratio for pile foundations of offshore wind turbines (OWTs), the other is the effects of pile diameter and aspect ratio on the design of pile foundations of OWTs. It is believed that the three-dimensional (3D) finite element (FE) analysis is the most accurate and reliable approach to address the soil-pile interaction of the monopile supported wind turbines. However, it is time-consuming to build the 3D FE models for so many (i.e., 100) wind turbines in a wind farm in the areas (i.e., Japan) where the soil stratum is very complicated and varies from site to site. In addition, the 3D FE analysis is not suitable for the integrated analysis of wind turbines that are needed for the design and control of wind turbines under multi-hazards such as wind, wave, and earthquake. Therefore, the concept of a simplified 1D model is applied to overcome the limitations of the 3D FE analysis.

In terms of how to consider the effects of pile diameter and aspect ratio, three representative approaches were proposed. The first approach is to propose the empirical formulae based on 3D FE analyses.

* Corresponding author.
E-mail addresses: lilin.wang@bridge.t.u-tokyo.ac.jp (L. Wang), ishihara@bridge.t.u-tokyo.ac.jp (T. Ishihara).

https://doi.org/10.1016/j.oceaneng.2022.110874
Received 24 July 2021; Accepted 18 February 2022
Available online 9 March 2022

In the PISA project (Byrne et al., 2019a), the PISA 1D model was developed for the design of monopiles using the soil reaction curves extracted from 3D FE analyses. The empirical formulae were also proposed for 4 types of soil reactions in the PISA 1D model by identifying 16 parameters with a limited parameter space (Beuckelaers, 2017). Based on the findings about 3D FE analyses in the PISA project, a new application called MoDeTo (Monopile Design Tool) (Minga and Burd, 2018), developed as a satellite tool of the Finite Element software PLAXIS 3D (Plaxis, 2019), was created to facilitate the design of monopiles of OWTs (Panagoulias and Hosseini, 2018). Although these methods are powerful, they heavily rely on 3D FE analyses. It is very time-consuming to run a great many 3D FE analyses. The second approach is based on the configuration of the PISA 1D model. Some researches proposed new models by removing one or two soil reaction curves in the PISA 1D model. Zhang and Andersen (2019) proposed the new lateral resistance and base shear models for the monopile foundation in pure clay without considering the distributed moment curves and base moment curve. Wang et al. (2020b) proposed a three-spring model for soft clay without considering the distributed moment curves. Fu et al. (2020) proposed another three-spring model for soft clay without considering the base moment curve. These models were proposed for pure clay, which is not enough for real monopiles in layered soils. In addition, Taghavi et al. (2020) proposed new models for the side, lateral, and rotational soil reactions to investigate the coupling of axial and lateral resistances for the large-diameter drilled shaft in Florida limestone, in which the pile tip effects are omitted. However, these simplifications may reduce the universality of the PISA 1D model. It is noted that some researches (e.g. He et al., 2019a, 2019b, 2021) also derived the rigorous solutions for the three-dimensional interactions of the soil and monopile based on the dynamic Biot's theory or Green's functions, in which the numerical simulations were performed for pure sand or clay and the validation and application to real monopiles in layered soils were not discussed. The third approach is to modify the existing p-y curves or to propose new p-y curves to account for the effects of pile diameter and aspect ratio (e.g. Wiemann et al., 2004; Sørensen et al., 2010; Sørensen, 2012; Kallehave et al., 2012; Thieken et al., 2015; Achmus et al., 2016; Wang et al., 2020a). DNVGL-RP-C212 (2017) also suggests using the p-y curves (e.g. API RP 2A-WSD, 2010) for the monopile design with necessary calibration by the 3D FE analysis.

Some researches were carried out to investigate the effects of pile diameter and aspect ratio on the design of pile foundations of OWTs. Ishihara and Wang (2019) built a linearized Winkler model using the initial stiffness and damping of the soil to estimate the modal properties of a Vestas V90 3 MW wind turbine. They found that the modal damping of the first mode was significantly underestimated. They stated that this may be due to the lack of consideration of the three-dimensional effects (the effects of pile diameter and aspect ratio) of monopiles. An accurate estimation of the modal damping is necessary for the efficient design of OWTs. As one of the main sources of the overall damping of OWTs, the foundation damping is the least well understood. As stated in Malekjafarian et al. (2021), one of the main remaining challenges for accurately determining foundation damping of OWTs is the lack of a widely accepted or industry standard integrated structural geotechnical methodology for the accurate determination of foundation damping. They also pointed out that simple models to define the soil damping effects for various foundation types, soil conditions and loading types are needed in the early stage of design. This study contributes to this issue.

This study focuses on how to derive the 1D model with the emphasis of considering coupling between axial and lateral resistances. A semi-analytical 1D mode is derived from the fishbone frame model to investigate the effects of the pile diameter and aspect ratio of offshore pile foundations. Although the static soil reactions are used in this study, the concept of the semi-analytical 1D model can also be applied to solve the cyclic soil-pile interactions with the proper determination of the soil reactions. The common approach to model the cyclic soil reactions in engineering is applying a cyclic factor to the static soil reactions, see API RP 2A-WSD, 2010. The outline of this paper is given as follows: the configuration of the semi-analytical 1D model, proposal of the soil reaction curves, identification and validation of the correction factor are presented in Section 2. Verification of the proposed model for monopiles in layered soils and investigation of the coupling between axial and lateral resistances on the modal damping of the monopile supported wind turbine in layered soils are performed in Section 3. Conclusions are given in Section 4.

2. A semi-analytical 1D model for pile foundations

A semi-analytical 1D model is derived from the fishbone frame model in Section 2.1. The soil reaction models for the semi-analytical 1D model are proposed in Section 2.2. The identification and validation of the correction factor are described in Section 2.3.

2.1. Configuration of the semi-analytical 1D model

The derivation of the semi-analytical 1D model for pile foundations is demonstrated using a monopile under the combined loading (F, M, V, T). F, M , V and T represent the horizontal force, the rotational moment, the axial force, and the torsional force, respectively. V could be the gravity of the superstructure. Fig. 1 illustrates the configuration of a monopile under the combined loading, the stress distribution, and the soil-structure interaction models. More specifically, Fig. 1a shows the image of a 3D monopile under the combined loading (F, M, V, T) in the Cartesian coordinate system (x, y, z). In this study, the monopile is considered as an open-ended pile with a soil plug formed in the installation. The base capacity of monopiles with the soil plug is investigated in detail in Liu et al. (2016) and Wang et al. (2018). This study adopts the Chinese method (Chinese Department of Construction, 2008) and the Finn method (FinnRA, 2000) to calculate the base capacity with a reduction factor to consider the effect of soil plug as shown in Appendix A. Correspondingly, the stresses acting onto the monopile due to soil reactions are depicted in Fig. 1b with a cylindrical coordinate system (r, α, z). In Fig. 1b, D is the diameter of the monopile, L_{all} is the length of the monopile, L is the embedment of the monopile, h is the load eccentricity of the monopile, σ_{r} and σ_{z} are the normal stresses while $\tau_{\text{r}\alpha}$, τ_{rz}, $\tau_{\text{z}\alpha}$ and τ_{zr} are the shear stresses acting on the pile shaft. Fig. 1c illustrates the fishbone frame model for the monopile, in which 6 types of soil reactions are employed to represent the soil reactions by decomposing the stresses in the horizontal, axial, and torsional directions. Note that the fishbone modeling concept was widely-used to model the bridge deck (see Xu and Wu (2007)) and the moment resisting frame (Khaloo and Khosravi, 2013). Fig. 1d represents an equivalent 1D model that derived from the fishbone frame model, in which the soil reaction curves are captured by 8 types of soil reactions as follows:

The $p_y - v_y$ spring depicts the relationship between the distributed lateral load applied to the pile shaft and the corresponding lateral pile displacement. The distributed lateral load is associated with σ_{r} and $\tau_{\text{r}\alpha}$ that are relevant to F.

The $S_{y,\,\text{pb}} - v_{y,\text{pb}}$ spring depicts the relationship between the shear force and the lateral displacement at the pile base. The base shear force is associated with $\tau_{z\alpha}$ and τ_{zr} that are relevant to F.

The $M_x - \theta_x$ spring depicts the relationship between the distributed moment applied to the pile shaft and the corresponding rotational pile displacement. The distributed moment is associated with τ_{rz} that is relevant to F and M.

The $M_{x,\,\text{pb}} - \theta_{x,\,\text{pb}}$ spring depicts the relationship between the moment and the rotation at the pile base. The base moment is associated with σ_z that is relevant to F and M.

The $t_z - v_z$ spring depicts the relationship between the distributed axial friction and displacement along the pile shaft. The distributed axial friction is associated with τ_{rz}^0 that is relevant to V. τ_{rz}^0 represents the shear

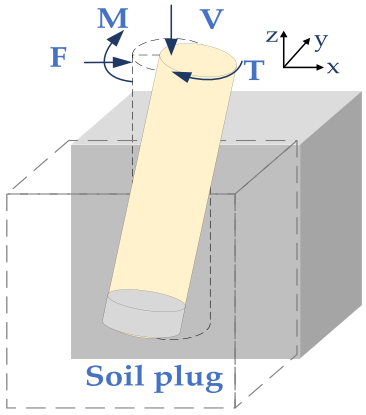

(a) Monopile with loading

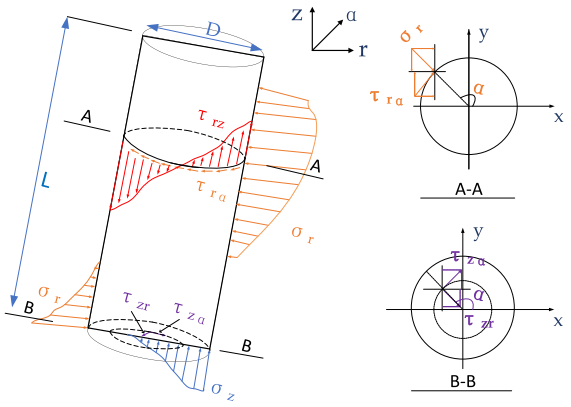

(b) Indication of stress on monopile from soil

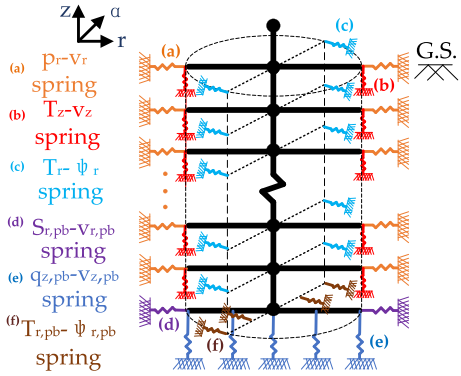

(c) Fishbone frame model (6 types of springs)

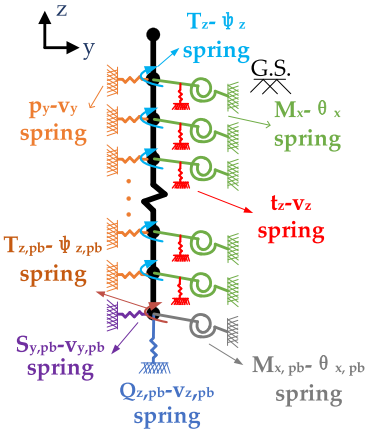

(d) Semi-analytical 1D model (8 types of springs)

Fig. 1. Configuration of loading, stress distribution, and soil-structure interaction models for a monopile (G.S. stands for ground surface, pb stands for pile base).

stress caused by V while τ_{rz} represents that caused by F and M.

The $Q_{z,\,pb} - v_{z,\,pb}$ spring depicts the relationship between the base axial resistance and the displacement of the pile base. The base moment is associated with σ_z^0 that is relevant to V. σ_z^0 represents the normal stress caused by V while σ_z represents that cause by F and M.

The $T_z - \varphi_z$ spring depicts the relationship between the distributed torque applied to the pile shaft and the corresponding torsional pile displacement. The distributed torque is associated with $\tau_{r\alpha}^0$ that is relevant to T. $\tau_{r\alpha}^0$ represents the shear stress caused by T while $\tau_{r\alpha}$ represents that caused by F.

The $T_{z,\,pb} - \varphi_{z,pb}$ spring depicts the relationship between the torque and the torsional displacement at the pile base. The base shear force is associated with $\tau_{z\alpha}^0$ that are relevant to T. $\tau_{z\alpha}^0$ represents the shear stress caused by T while $\tau_{z\alpha}$ represents that caused by F.

The restoring forces of the 8 types of soil reactions can be easily derived based on the stress distribution around the pile, which can be expressed as Eqs. (1)–(8).

$$p_y(z) = \int_0^{2\pi} (\sigma_r \cos\alpha + \tau_{r\alpha} \sin\alpha)\frac{D}{2} d\alpha \tag{1}$$

$$M_x(z) = \int_0^{2\pi} \tau_{rz}(\alpha)\left(\frac{D}{2}\right)^2 \cos\alpha d\alpha \tag{2}$$

$$S_{y,pb} = \int_0^{D/2}\int_0^{2\pi} (\tau_{zr} \cos\alpha + \tau_{z\alpha} \sin\alpha) r d\alpha dr \tag{3}$$

$$M_{x,pb} = \int_0^{D/2}\int_0^{2\pi} (\sigma_z \cos\alpha) r^2 d\alpha dr \tag{4}$$

$$t_z(z) = \tau_{rz}^0 \pi D \tag{5}$$

$$Q_{z,pb} = \sigma_z^0 \frac{\pi}{4} D^2 \tag{6}$$

$$T_z(z) = \tau_{r\alpha}^0 \pi D \tag{7}$$

$$T_{z,pb} = 2\pi \int_0^{D/2} \tau_{z\alpha}^0 r^2 dr \tag{8}$$

where $p_y(z)$, $M_x(z)$, $S_{y,pb}$, $M_{x,pb}$, $t_z(z)$, $Q_{z,pb}$, $T_z(z)$ and $T_{z,pb}$ are the restoring forces of the $p_y - v_y$ spring, the $M_x - \theta_x$ spring, the $S_{y,\,pb} - v_{y,pb}$ spring, the $M_{x,\,pb} - \theta_{x,\,pb}$ spring, the $t_z - v_z$ spring, the $Q_{z,\,pb} - v_{z,\,pb}$ spring, the $T_z - \varphi_z$ spring and the $T_{z,pb} - \varphi_{z,pb}$ spring, respectively. z represents the spring depth ($0 \le z \le L$), α represents the angle variable ($0 \le \alpha \le 2\pi$) while r represents the radius variable ($0 \le r \le D/2$).

2.2. Proposal of soil reaction models for the semi-analytical 1D model

There are eight constituent reaction relationships for modeling pile foundations in the proposed semi-analytical 1D model. That is, in addition to commonly used relationships for modeling lateral resistance ($p_y - v_y$), axial (side) resistance ($t_z - v_z$), and toe axial end-bearing

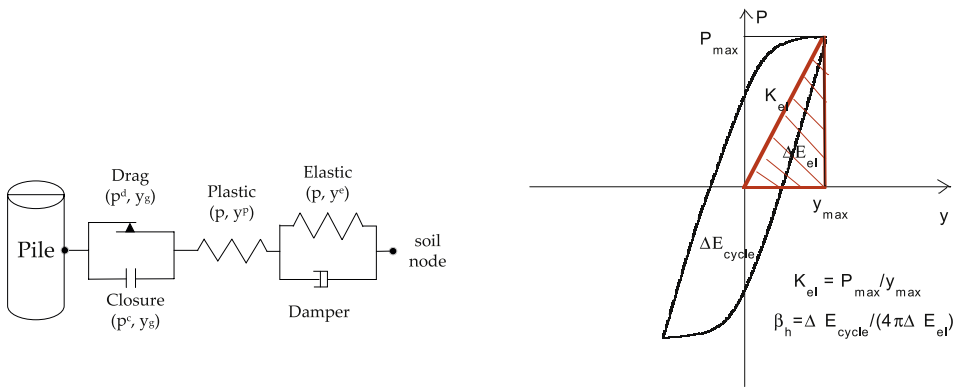

(a) Configuration of PySimple1 (b) Hysteresis loop of PySimple1

Fig. 2. Configuration and hysteresis loop of PySimple1.

($Q_{z,\,pb} - v_{z,\,pb}$), other relationships might be used to model torsional resistance along the length of the pile ($T_z - \varphi_z$), torsional resistance at the pile base ($T_{z,\,pb} - \varphi_{z,pb}$), rotational resistance ($M_x - \theta_x$) along the length of the pile due to the axial and lateral resistance coupling, base overturning resistance at the tip of the pile ($M_{x,\,pb} - \theta_{x,\,pb}$), and base shear resistance at the tip of the pile ($S_{y,\,pb} - v_{y,pb}$). As stated in Taghavi et al. (2020), utilizing each of these resistance relationships (soil reactions) depends on the geometry of the pile, loading regime, and geotechnical site conditions. $T_z - \varphi_z$ and $T_{z,\,pb} - \varphi_{z,pb}$ are only needed in cases where members are subjected to torsional loading (Randolph, 1981). When analyzing large-diameter monopiles to support wind turbines, the deep foundation may be subjected to high overturning moments, the rotational resistance ($M_x - \theta_x$) along the length of the pile, the base overturning resistance ($M_{x,\,pb} - \theta_{x,\,pb}$) and the base shear resistance ($S_{y,\,pb} - v_{y,pb}$) matter. However, in the cases with small-diameter piles such as jackets and pile groups, only $p_y - v_y$, $t_z - v_z$, and $Q_{z,\,pb} - v_{z,\,pb}$ are needed. In this study, the $p_y - v_y$ and $t_z - v_z$ models are modeled as PySimple1 (Boulanger, 2000) and TzSimple1 (Boulanger, 2000); the $S_{y,\,pb} - v_{y,pb}$ and $Q_{z,pb} - v_{z,pb}$ models are modeled as TzSimple2 (Raychowdhury and Hutchinson, 2009) and QzSimple2 (Raychowdhury and Hutchinson, 2009). This is because PySimple1, TzSimple1 and QzSimple1 were proposed for the small-diameter pile foundation (Boulanger et al., 2002) and recalibrated to PySimple2, QzSimple2 and TzSimple2 for the gravity foundation (Raychowdhury and Hutchinson, 2009). It is noted that only slight difference exists between TzSimple1 and TzSimple2, and so does for QzSimple1 and QzSimple2. The $M_x - \theta_x$ model reflects the contribution of vertical skin friction to the lateral resistance of large-diameter piles (Ashour and Helal, 2014) and can also be modeled using TzSimple1. The $M_{x,\,pb} - \theta_{x,\,pb}$ model reflects the contribution of toe axial ending bearing to the lateral resistance of large-diameter piles and can be modeled using QzSimple2. Li (2017) proposed the torsional resistances using the hyperbolic function by fitting to the field experiments, which is used to model the $T_z - \varphi_z$ and $T_{z,\,pb} - \varphi_{z,pb}$ models in this model. The soil reactions are demonstrated using PySimple1 whose configuration and hysteresis loop are shown in Fig. 2. The governing equations of PySimple1 can be found in Appendix A, in which Eq. (A3) shows that the unloading and reloading are achieved by updating the reversal point (y_0^p, p_0) in the plastic component of PySimple1. The hysteretic soil damping can be calculated from the hysteresis loop of PySimple1 using Eq. (9).

$$\beta_h = \frac{\Delta E_{\text{cycle}}}{4\pi \Delta E_{\text{el}}} \tag{9}$$

where ΔE_{cycle} is the damping energy and ΔE_{el} is the equivalent elastic strain energy.

As summarized in Table 1, there are two parameters for each soil reaction including the ultimate bearing capacity and a representative displacement (the displacement corresponding to a half of the ultimate bearing capacity). The calculations of input parameters can also be found in Appendix A, in which a correction factor κ is introduced for the calculation of the ultimate bearing capacities of the lateral and rotational soil reactions on the pile shaft. Eq. (10) shows the proposal of σ_{r0} based on the Rankine's theory, in which κ represents the correction factor accounting for the three-dimensional effect of the passive wedge formed in front of pile foundations. A similar correction factor can be

Table 1
Models and parameters for the soil reactions in the semi-analytical 1D model.

Soil spring	Material in OpenSees	Ultimate bearing capacity	Representative displacement
$p_y - v_y$	PySimple1	$p_{ult}(z)$	$y_{50}(z)$
$M_x - \theta_x$	TzSimple1	$M_{ult}(z)$	$\theta_{50}(z)$
$S_{y,\,pb} - v_{y,pb}$	TzSimple2	$S_{ult,pb}$	$y_{50,pb}$
$M_{x,\,pb} - \theta_{x,\,pb}$	QzSimple2	$M_{ult,pb}$	$\theta_{50,pb}$
$t_z - v_z$	TzSimple1	$t_{ult}(z)$	$z_{50}(z)$
$Q_{z,\,pb} - v_{z,\,pb}$	QzSimple2	$Q_{ult,pb}$	$z_{50,pb}$
$T_z - \varphi_z$	Hyperbolic function[a]	$T_{ult}(z)$	$\varphi_{50}(z)$
$T_{z,pb} - \varphi_{z,pb}$	Hyperbolic function[a]	$T_{ult,pb}(z)$	$\varphi_{50,pb}(z)$

[a] Hyperbolic function from Li (2017): $T = \dfrac{\varphi}{\dfrac{1}{K_T} + \dfrac{\varphi}{T_{\text{ult}}}}$, T_{ult} and K_T are the ultimate capacity and initial stiffness, respectively.

Table 2
Summary of soil properties in PISA project.

Test Site (−)	Soil type (−)	Ground water table (m)	Unit weight (kN/m^3)	Poisson ratio (−)	Friction angle (deg)
Dunkirk	Dense sand	−5.4	17.1/19.9	0.2	33
Cowden	Stiff clay	−1	21.19	0.5	–

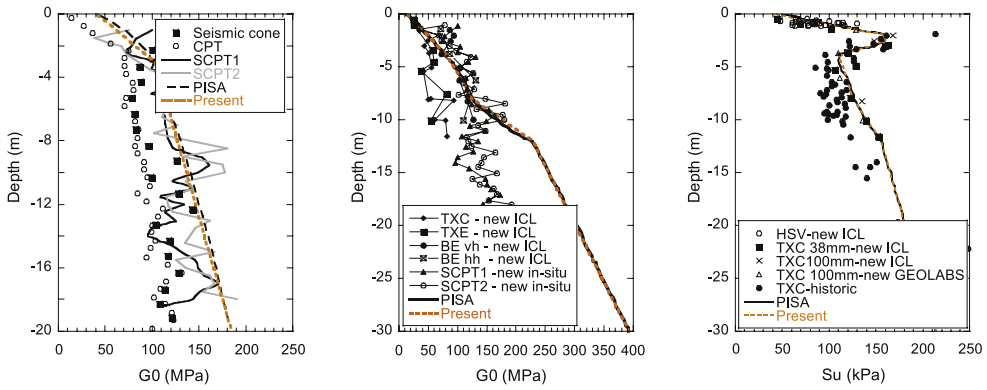

(a) Initial shear modulus of dense sand at Dunkirk (b) Initial shear modulus of stiff clay at Cowden (c) Undrained shear strength of stiff clay at Cowden

Fig. 3. Initial shear modulus and undrained shear strength of sand and clay in PISA project.

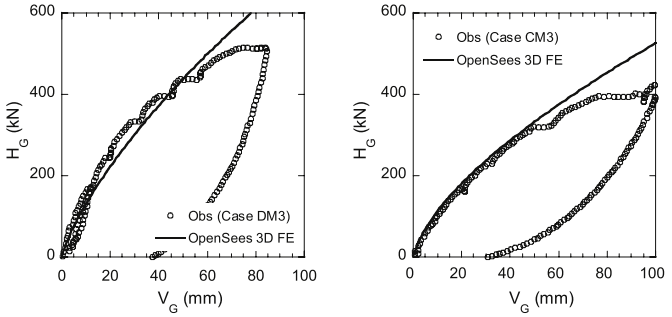

(a) Case DM3 (b) Case CM3

Fig. 4. Validation of the OpenSees 3D FE analyses.

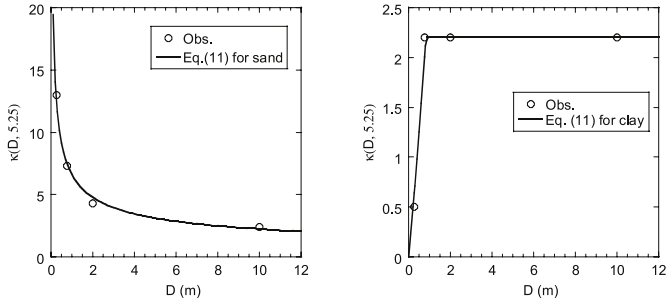

(a) Sand (b) Clay

Fig. 5. The effects of pile diameter on κ for both sand and clay ($L/D = 5.25$).

found in Gerolymos and Gazetas (2006). How to determine the value of κ is discussed in Section 2.3.

$$\sigma_{r0} = \kappa\left(2c\sqrt{K_p} + \gamma' z K_p\right) \tag{10}$$

2.3. Identification and validation of correction factor in the semi-analytical 1D model

The PISA project combined ground characterisation, field testing, and computational analysis to develop new design models for large-diameter monopiles of offshore wind turbines (Byrne et al., 2019a, 2019b, 2020; Zdravković et al., 2019a, 2019b; McAdam et al., 2019; Taborda et al., 2019; Burd et al., 2020). The soil information for the dense marine sand at Dunkirk and the stiff glacial clay till at Cowden are summarized in Table 2 and Fig. 3. Data from the PISA project or the 3D FE analyses performed by authors are employed to identify the correction factor for the proposed model. The reason why the 3D FE analyses can be used to identify the correction factor is that the predictions by 3D FE analyses were found to be close to the experimental results in PISA project (Byrne et al., 2019a). In this study, the 3D FE analyses by authors are conducted in OpenSees (McKenna, 2011) and visualized by the open-source interface OpenSeesPL (Lu et al., 2011), which are called OpenSees 3D FE to distinguish from those in PISA project. The soil constitutive models, parameters, soil meshes, and solvers are shown in Appendix B. As shown in Fig. 4, OpenSees 3D FE analyses are validated against PISA experiments using Case DM3 for sand and Case CM3 for

Table 3
Geometrical properties and load eccentricities of tested piles in PISA project.

Case	Pile diameter	Pile configuration at Dunkirk			Pile configuration at Cowden			Data source
	D	L/D	h/D	t/D	L/D	h/D	t/D	
S1	0.273 m	5.25	18.3	0.0256	5.25	18.32	0.0256	PISA
M2	0.762 m	5.25	13.1	0.0174	5.25	13.10	0.0144	PISA
M3		8	13.2	0.0328	10	13.14	0.0328	PISA
M4		15	13.2	0.0328	15	13.14	0.0328	OpenSees
M5		20	13.2	0.0328	20	13.14	0.0328	OpenSees
M6		25	13.2	0.0328	25	13.14	0.0328	OpenSees
M7		30	13.2	0.0328	30	13.14	0.0328	OpenSees
M8		35	13.2	0.0328	35	13.14	0.0328	OpenSees
M9		40	13.2	0.0328	40	13.14	0.0328	OpenSees
L1	2 m	5.25	9.90	0.019	5.25	10.10	0.0125	PISA
SL1	10 m	6	5	0.01	6	5	0.01	PISA

Note: DS1 means the case of S1 for the pile configuration at Dunkirk and CS1 denotes the case of S1 for the pile configuration at Cowden. Others are named in a similar way. *OpenSees 3D FE is described in* Appendix B. t in Table 3 means the thickness of pile.

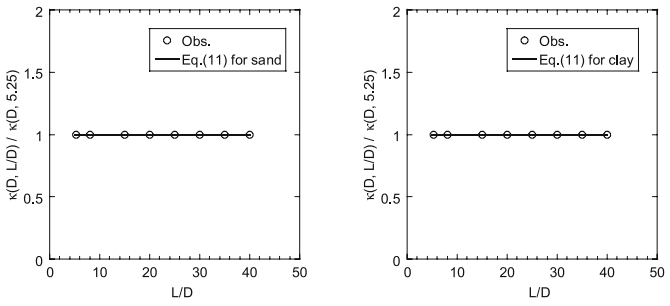

(a) Sand (b) Clay

Fig. 6. The effects of pile aspect ratio on κ for both sand and clay (D =0.762 m).

clay, in which V_G represents the displacement at the ground and H_G represents the corresponding loading acting on piles. Note that DM3 means the case of M3 for the pile configuration at Dunkirk and CM3 denotes the case of M3 for the pile configuration at Cowden. The configurations of pile geometrical properties and load eccentricities are presented in Table 3.

The correction factor κ in Eq. (11) is introduced to calculate the ultimate bearing capacity of PySimple1 and TzSimple1, which is identified for sand and clay using a curve-fitting approach. Effects of the pile diameter and aspect ratio on κ are investigated using the control variate method (Wikipedia). The pile diameter effect is investigated by controlling L/D as 5.25, while the pile aspect ratio effect is examined by controlling D as 0.762 m. The fitting of $\kappa(D, 5.25)$ includes two steps. The first step is performed to obtain the observed data in Fig. 5 for the 4 sand cases in Fig. 7 and the 4 clay cases in Fig. 8, which is conducted manually since running OpenSees is needed. The experimental data points corresponding to the displacements of 0.01D, 0.025D, 0.05D, 0.075D, and 0.1D in the load-displacement curves are used in the first step. The second step is performed to obtain the formulae of $\kappa(D, 5.25)$ by fitting to the observed data in Fig. 5, which is conducted automatically. In the fitting process, the least-squares method is adopted with the objective function of the sum squared residual. The fitting of $\kappa(D, L/D)/\kappa(D, 5.25)$ can be conducted similarly as shown in Fig. 6. The multiply product of the formulas of $\kappa(D, 5.25)$ and that of $\kappa(D, L/D)/\kappa(D, 5.25)$ are given in Eq. (11). Note that selecting the cases of $L/D = 5.25$ and $D = 0.762$m for the calibration of the κ is based on the data available.

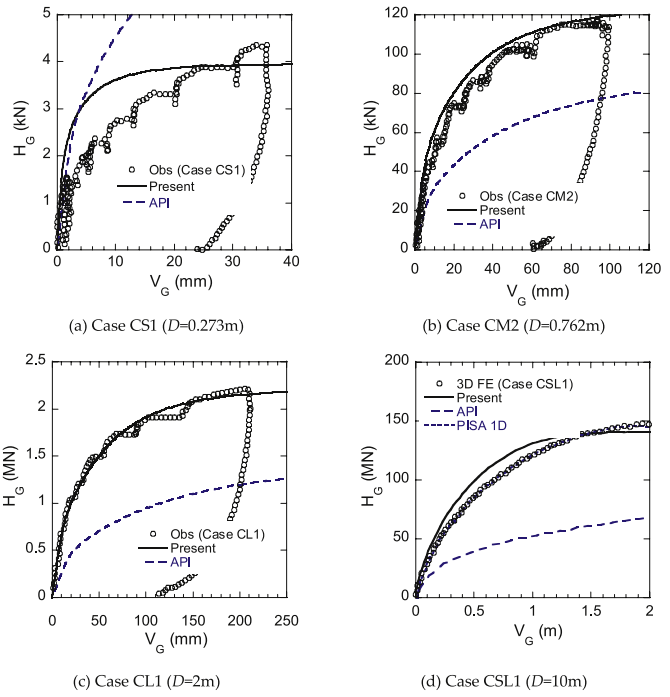

(a) Case CS1 (D=0.273m) (b) Case CM2 (D=0.762m)

(c) Case CL1 (D=2m) (d) Case CSL1 (D=10m)

Fig. 8. Comparison of measured and predicted load-displacement curves for various pile diameters in clay (L/D = 5.25).

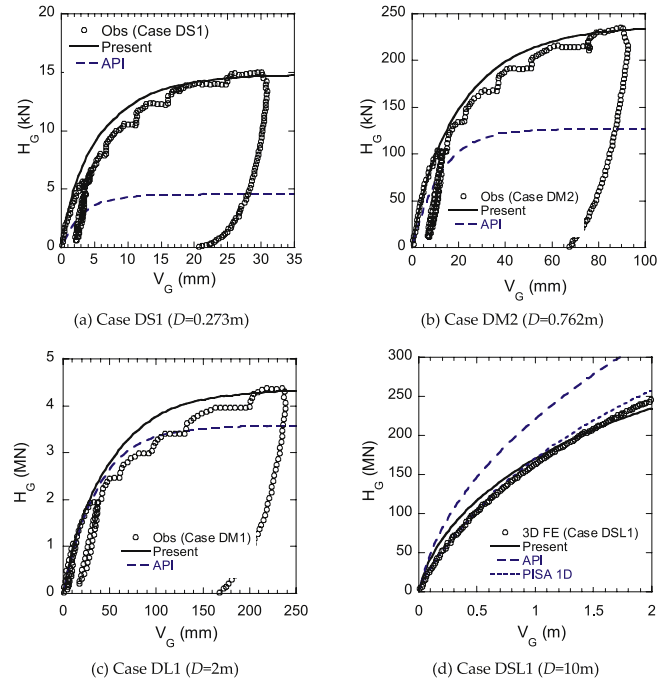

(a) Case DS1 (D=0.273m) (b) Case DM2 (D=0.762m)

(c) Case DL1 (D=2m) (d) Case DSL1 (D=10m)

Fig. 7. Comparison of measured and predicted load-displacement curves for various pile diameters in sand (L/D = 5.25).

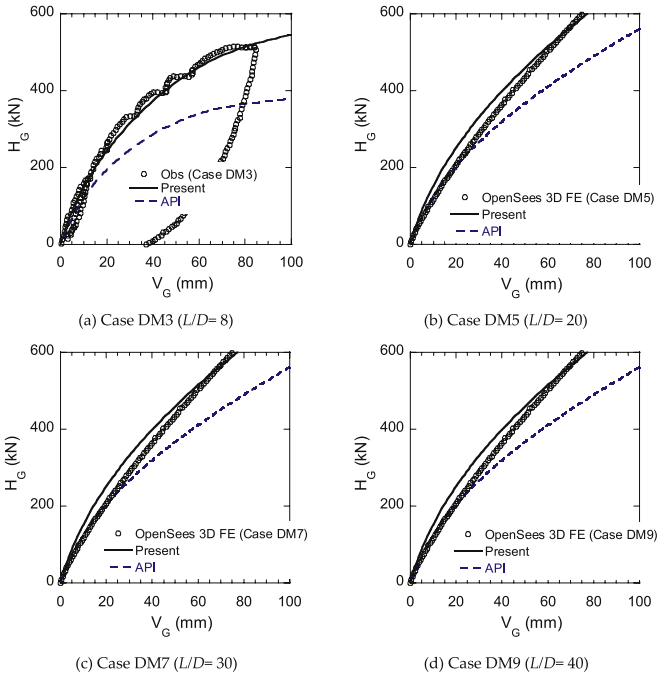

(a) Case DM3 (L/D= 8) (b) Case DM5 (L/D= 20)

(c) Case DM7 (L/D= 30) (d) Case DM9 (L/D= 40)

Fig. 9. Comparison of measured and predicted load–displacement curves for various pile aspect ratios in sand (D = 0.672m).

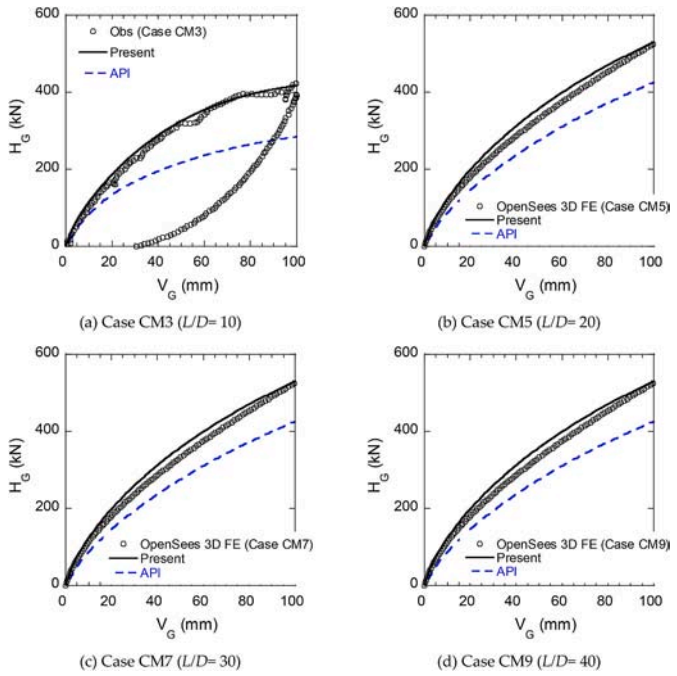

Fig. 10. Comparison of measured and predicted load-displacement curves for various pile aspect ratios in clay (D = 0.672m).

$$\kappa(D,L/D)=\frac{\kappa(D,L/D)}{\kappa(D,5.25)}\cdot\kappa(D,5.25)=\begin{cases}6.612\cdot D^{-0.469} & \text{for sand}\\ \min\left(2.714\cdot D^{1.112},\ 2.2\right) & \text{for clay}\end{cases} \tag{11}$$

Fig. 5 shows the dependence of κ on the pile diameter. It is observed that for the case with a larger pile diameter (e.g. more than 2 m), κ varies slightly with the pile diameter and approaches to a constant value. It is to be noted that when $\kappa = 3$ for sand and $\kappa = 2.2$ for clay are used, the validation metrics can be satisfied for the pile diameter larger than 2 m. However, for the case with a small pile diameter, κ varies significantly.

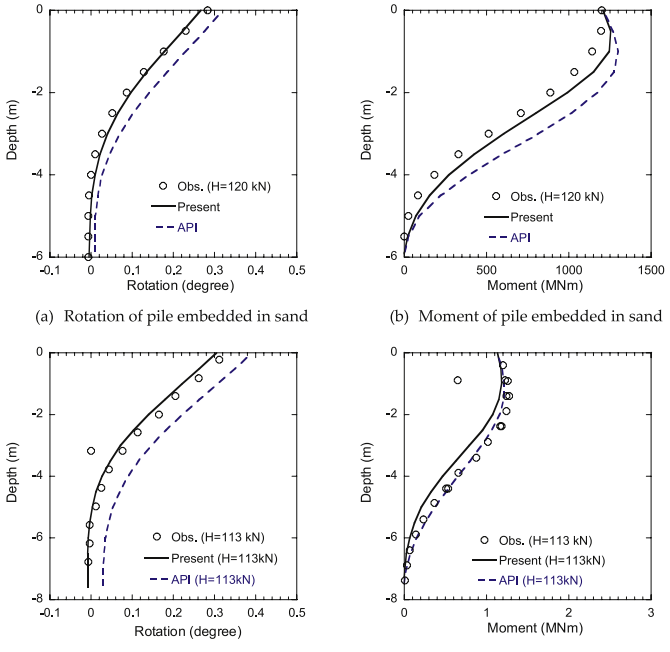

Fig. 11. Comparison of predicted and measured pile responses for the cases of DM3 and CM3 with D = 0.762 m and L/D = 8 for sand, L/D = 10 for clay.

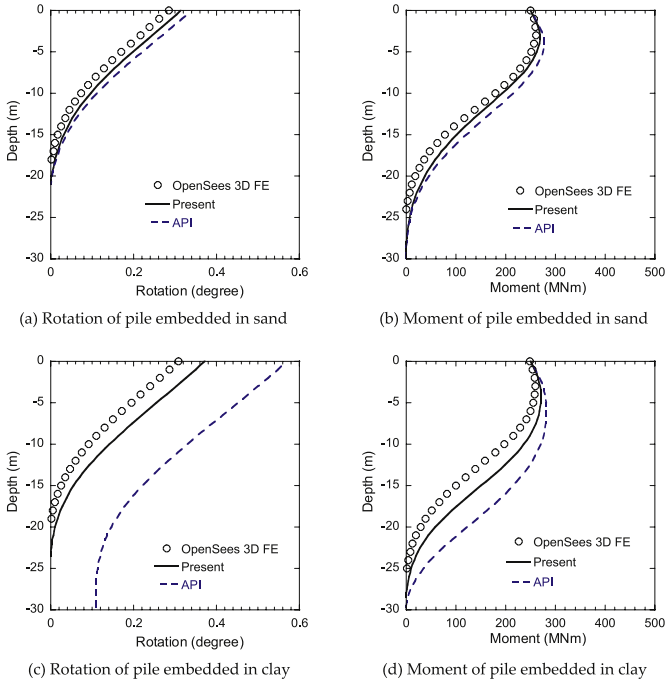

Fig. 12. Comparison of predicted and measured pile responses for the cases with D = 5 m and L/D = 6.

Table 4
Summary of soil properties of two idealized homogenous soils.

Site	Soil type	Ground water table (m)	Unit weight (kN/m^3)	Poisson ratio (−)	Friction angle (deg)	Undrained shear strength (MPa)
Dunkirk	Dense sand	0	19.8	0.2	39	–
Cowden	Stiff clay	0	17.8	0.5	–	G_0/1363.6

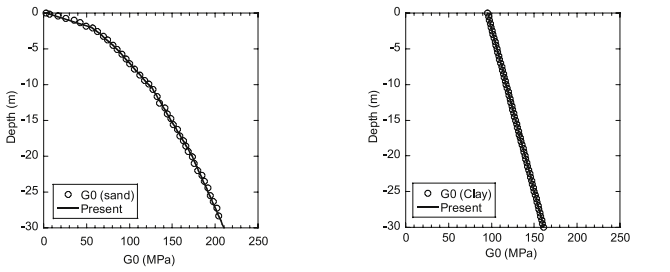

(a) Initial shear modulus of dense sand (case S)

(b) Initial shear modulus of stiff clay (case C)

Fig. 13. Initial shear modulus for Case S and Case C (Panagoulias et al., 2019).

The reason is that the ultimate capacity $p_{ult}(z)$ is expressed as the function of the Rankine's passive pressure coefficient but the assumption of Rankine's theory cannot be not satisfied at all for the case with a small pile diameter. Similar non-dimensionalised conditions are also used in Yoo et al. (2013) and Lim and Jeong (2018) when applying the Rankine's passive pressure coefficient to calculate the ultimate capacity of the p-y curve for a small pile diameter (e.g. 1 m). Fig. 6 depicts the dependence of κ on the pile aspect ratio. It is noticed that the pile aspect ratio influences the correction factor little. This is because the effects of the pile aspect ratio is covered by the soil reactions at the pile base.

During the identification of the correction factor κ, a series of static numerical analyses are conducted in OpenSees (McKenna, 2011) for the cases as shown in Table 3. The monopile is modeled by Timoshenko beams with a length of 0.5 m. The mass of the monopile is modeled by a series of lumped masses at the beam joints. Conventional steel material properties with Young's modulus of 205 GPa and the Poisson's ratio of 0.3 are employed. The soil-pile interaction is modeled by 8 types of soil reactions in the proposed model with 0.5-m intervals. The soil properties (e.g. initial shear modulus and undrained shear strength) are linearized for each 0.5 m interval. For example, the initial shear modulus at -1.5 m is used for the range of -1.25~-1.75 m. The analyses are conducted by first applying gravity loading using a constant axial load, and subsequently imposing a horizontal load. The load is imposed incrementally using a static load control integrator, with the size of the increments depending on the nonlinearity in the foundation response. Force convergence is obtained when the norm of the displacement residuals was smaller than a specified tolerance, i.e. 10^{-5}. Penalty constraints are used to enforce the prescribed displacement boundary conditions. The numbering of nodal degrees of freedom is performed using a reverse Cuthill-McKee algorithm and the system of equations is set up and solved using a Newton-Raphson algorithm.

The proposed model with the correction factor in Eq. (11) is then evaluated by PISA experiments for the cases with the same pile aspect ratio but different pile diameters. Fig. 7 depicts the comparisons of the predicted and measured load-displacement curves at the ground level for the dense sand at Dunkirk. It is noticed that the predictions by the proposed model show good agreements with the experiments (known as Obs. or 3D FE) for sand. Fig. 8 portrays the comparisons of the predicted and measured load-displacement curves at the ground level for the stiff clay at Cowden. It is found that the predictions by the proposed model also show good agreements with the experiments for clay. Note that the proposed model does not agree well with experiments for large displacements of Case CS1. The differences for Case CS1 may be related to the very small penetration depths in combination with the irregular undrained shear strength profile at Cowden. The predictions by the API model are also added in Figs. 7 and 8. However, the API model significantly underestimates or overestimates the load-displacement curves at the ground level due to the small pile aspect ratio ($L/D = 5.25$) for both sand and clay. Among the existing 1D models, the PISA 1D model is a pioneering research output which was exactly proposed for the soil-pile interaction of monopiles. It overcomes the limitations of the API model that was borrowed from the oil and gas industry since it models the coupling between the axial and lateral resistance as the rotational soil reactions. Currently, the concept of the PISA 1D model is widely used in the design of monopile supported wind turbines in Europe and other places in the world. Comparisons between the proposed model and the PISA 1D model can be stated as follows: i) the PISA 1D model is empirically fitted to the 3D FE analyses while the proposed model is analytically derived and calibrated by the 3D FE analyses, ii) 16 unknown parameters in the PISA 1D model need to be identified while only one identified parameter in the proposed model, which means the proposed model is simpler; iii) Due to more identified parameters used in the PISA 1D model, it shows slightly higher accuracy than the proposed model for some specific cases, see Figs. 7d and 8d.

The proposed model also works well for the cases with the same pile diameter but different pile aspect ratio, which can be found in Fig. 9 for the dense sand at Dunkirk and in Fig. 10 for the stiff clay at Cowden, respectively. The prediction by the API model significantly underestimates the load-displacement curve for the small pile aspect ratios (e.g. the relative error of -34% at the displacement of 0.1D for the pile aspect ratio of 8 in Fig. 9a). The API model shows better agreement with the numerical experiments for the large pile aspect ratios (e.g. the relative errors are reduced to −20% at the displacement of 0.1D for the pile aspect ratios of 20 in Figs. 9b and 30 in Figs. 9c and 40 in Fig. 9d). In summary, the proposed semi-analytical 1D model suits the cases with

Table 5
Description of geometrical properties of pile and load eccentricity.

D (m)	L (m)	h (m)	t (m)	L/D (−)	h/L (−)	D/t (−)
7	28	56	0.07	4.0	2.0	100.0

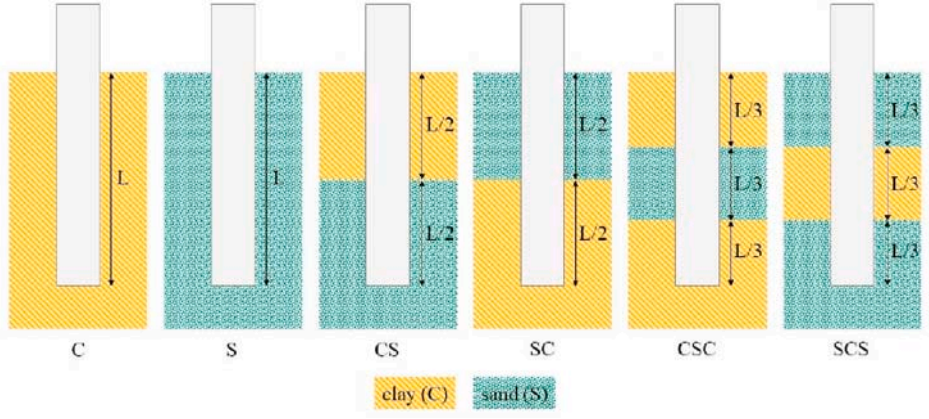

Fig. 14. Configuration of monopile embedded in six soil profiles (Panagoulias et al., 2019).

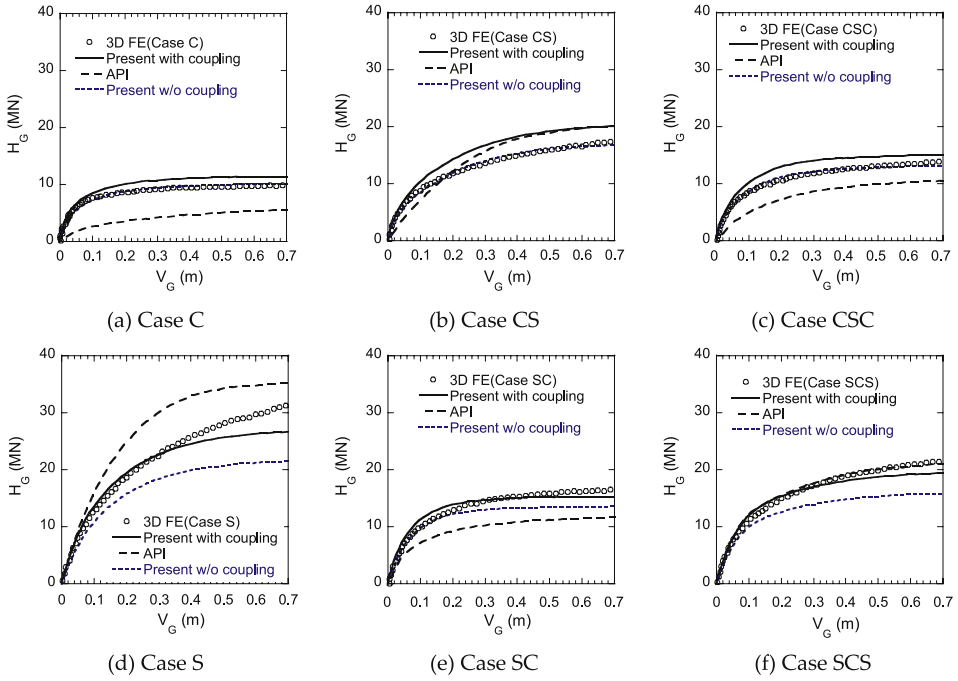

(a) Case C (b) Case CS (c) Case CSC

(d) Case S (e) Case SC (f) Case SCS

Fig. 15. Comparisons of predicted and measured load-displacement curves for layered soils.

various pile diameters and aspect ratios. It is noted that although the semi-analytical model is mainly calibrated for the lateral loading of monopiles, it can be applied to the coupled lateral, axial, and torsional loading since the coupling between axial and lateral resistance is modeled with the rotational soil reactions and no additional coupling effects need to be considered. In addition, the proposed model is also calibrated for slender piles as given in Figs. 9 and 10, which means it can be applied to jacket supported wind turbines and pile group supported wind turbines once the group effect is properly considered (see JSCE guideline (Ishihara, 2010)).

The proposed model is then validated for the rotation and moment responses of pile foundations. The comparisons of predicted and measured pile responses for small-diameter cases (e.g. the Case DM3 and Case CM3) and for large-diameter cases (e.g. the cases with a pile diameter of 5 m and a pile aspect ratio of 6) are given in Fig. 11 and Fig. 12, respectively. It is observed that the proposed model shows good

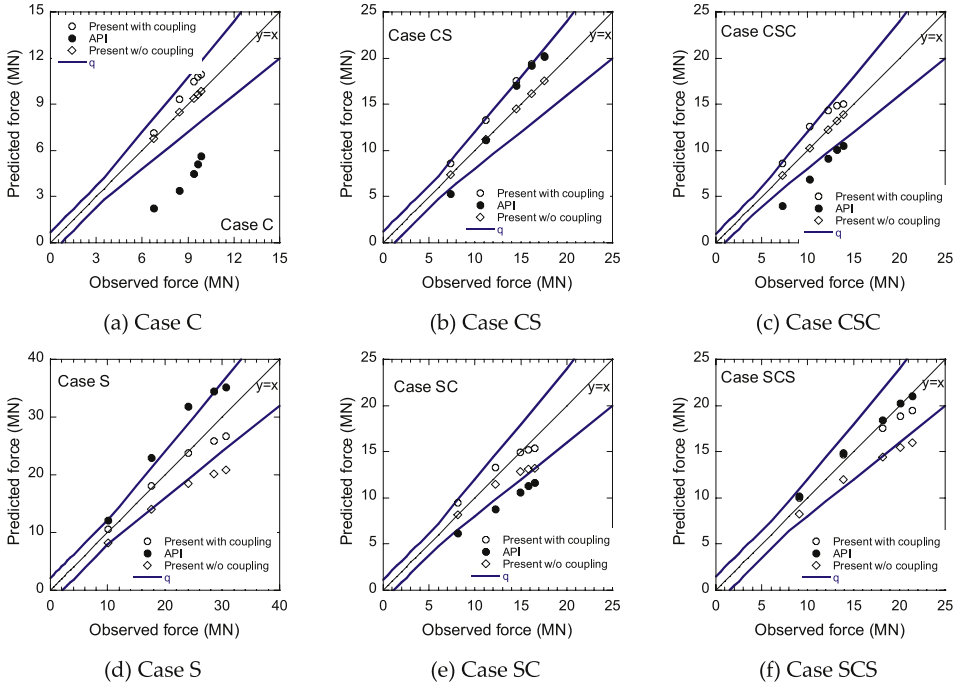

(a) Case C (b) Case CS (c) Case CSC

(d) Case S (e) Case SC (f) Case SCS

Fig. 16. Results of validation metrics for layered soils.

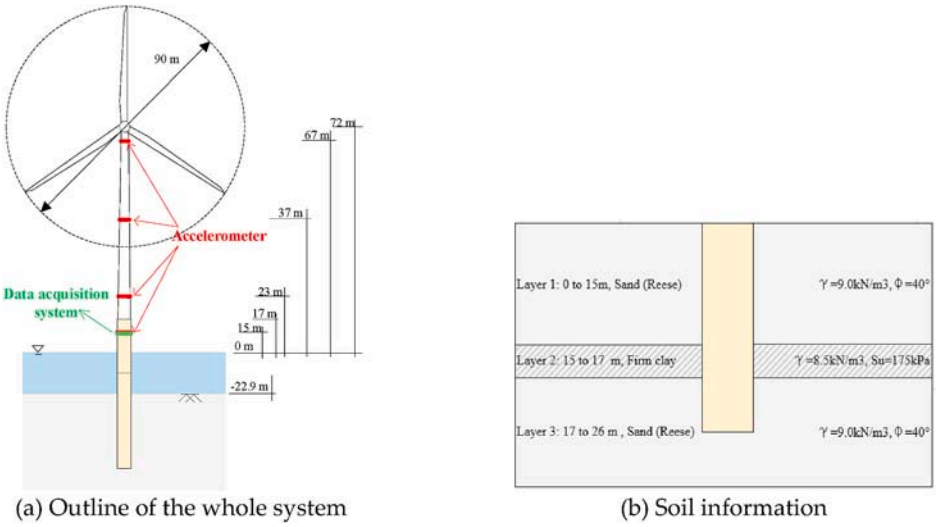

Fig. 17. Vestas 3 MW wind turbine supporting by monopile foundation.

Table 6
Summary of Vestas 3 MW wind turbine.

Description	Value
Rated power	3 MW
Hub height (above MSL)	72 m
Rotor, hub diameter	90 m, 2.32 m
Tower diameter, thickness	2.75–4.25 m, 0.013–0.025 m
Nacelle & rotor mass	109,800 kg
Tower mass	108,000 kg
Transition Piece length	22 m, 167000 kg
Mean sea level (MSL)	22.9 m
Pile diameter, wall thickness	5 m, 0.06 m
Pile embedded depth	26.0 m

agreements with measurements for the rotation and moment responses for both small and large pile diameters in sand and clay. Besides, the predictions by the API model are also added in Figs. 11 and 12. It is found that the API model overestimates the rotation and moment responses of pile foundation for both sand and clay.

3. Effects of coupling between axial and lateral resistances on the modal damping of monopile supported wind turbines in layered soils

The verification of the proposed model for monopiles in layered soils is performed in Section 3.1. The effects of coupling between axial and lateral resistances on the modal damping of monopile supported wind turbines in the layered soil are described in Section 3.2.

3.1. Verification of the proposed model for monopiles in layered soils

In real engineering, the pile foundations are usually supported by layered soils, for which the errors of the proposed model may be accumulated. That is why the proposed model is verified against the layered soils in this section. Consider two idealized homogenous soil profiles, which are stiff normally consolidated clay (Case C) and very dense sand (Case S). The properties of sand and clay are summarized in Table 4 and Fig. 13. According to Panagoulias et al. (2019), the layered soils can be formed by combining the sand and clay profiles. Four layered soil profiles are defined, such as clay over sand (Case CS), sand over clay (Case SC), clay over sand over clay (Case CSC), and sand over clay over sand (Case SCS). The configuration of a monopile embedded in six soil profiles is illustrated in Fig. 14. The geometrical properties of the monopile and the load eccentricity are given in Table 5. The 3D FE analyses in Panagoulias et al. (2019) are used to validate the proposed model. These 3D FE analyses ware performed in PLAXIS 3D (Plaxis, 2019), in which the stiff clay layers are modeled with the NGI-ADP constitutive model (Andresen and Jostad, 1999) and the sand layers are modeled with the HSsmall model (Benz, 2007).

A series of static analyses for the six soil profiles are carried out in OpenSees (McKenna, 2011) to verify the proposed model and compared to the API model. The numerical models and solution schemes are the same as those mentioned in section 2.3. The predicted load-displacement curves at the ground level by the proposed model are shown in Fig. 15 and compared to those from 3D FE analyses. It is found that the proposed model shows reasonable agreement with the 3D FE analyses while the API model underestimates or overestimates some cases significantly. To quantify the agreement between the results from numerical experiments and the proposed model, a hit rate q is introduced as the validation metric (see Schatzmann and Olesen (2010) and Oettl (2015)) and is defined by Eq. (12):

$$q = \frac{1}{N}\sum_{i=1}^{N} n_i, \quad n_i = \begin{cases} 1, & \left|\frac{y_i - x_i}{x_i}\right| \le D_q \text{ or } |y_i - x_i| \le W_q \\ 0, & \text{else} \end{cases} \tag{12}$$

where x_i and y_i are the values of loads corresponding to the displace-

Table 7
Summary of soil properties for the Vestas 3 MW wind turbine.

Soil type	Effective unit weight (kN/m^3)	Friction angle (deg)	Undrained shear strength (kPa)	Poisson ratio (−)	Other parameters
Dense sand	9.0	40	–	0.2	D_r = 80%
Stiff clay	8.5	–	175	0.5	OCR = 9, I_p = 300%[a]

[a] The overconsolidation ratio OCR and the plasticity index I_p are evaluated from undrained shear strength s_u. As summarized in Chanmee et al. (2017), OCR can be evaluated using $s_u/\sigma'_{v0} = S{\cdot}OCR^m$ in Ladd and Foott (1974) with the values of $m = 0.8$ and S = 0.22 in Ladd and DeGroot (2004). The plasticity index I_p is estimated by $s_u/\sigma'_{v0} \approx 0.11 + 0.0037 I_p$ following Chandler (2009).

Table 8
Predictions of modal frequencies and modal damping ratios.

Mode	Model	Modal frequency			Modal damping ratio		
		Measured (Hz)	Predicted (Hz)	Error (%)	Measured (%)	Predicted (%)	Error (%)
1st mode	API	0.361 ± 0.004	0.361	-1.0	0.85	0.52	-38.8
	Present w/o coupling		0.358	-1.9		0.70	-17.6
	Present with coupling		0.368	0.8		0.84	-1.2
2nd mode	API	1.560 ± 0.016	1.707	8.3	1.15[a]	0.79	-31.3
	Present w/o coupling		1.689	7.2		0.90	-21.7
	Present with coupling		1.730	9.7		1.14	-1.0

[a] This value was obtained without considering the radiation damping, and the modal damping ratios evaluated in this study can be used in the dynamic analyses for the fatigue limit state (FLS), the service limit state (SLS) and the ultimate limit state (ULS) as mentioned in the introduction.

ments of 0.01D, 0.025D, 0.05D, 0.075D, and 0.1D in the load-displacement curves at the ground level by the numerical experiments and the proposed model for the ith case, respectively. N is the total number of cases, D_q and W_q are the threshold. The values of the metric corresponding to the complete agreement and disagreement are $q = 1$ and $q = 0$, respectively. Following the German VDI guideline 3783-9 (VDI, 2005), the thresholds $D_q = 0.25$ and $W_q = 0.07 \sim 0.1|\max|$ can be used, as suggested by Schatzmann and Olesen (2010) and Oettl (2015). The thresholds $D_q = 0.2$ and $W_q = 0.07|\max|$ are used in this study, in which $|\max|$ is a maximum value supposed in the observation. These thresholds mean the relative error for large values should be smaller than 20% and the absolute error for small values should be smaller than $0.07|\max|$. A similar accuracy metric was used in PISA project when the 3D FE results are compared with the field tests.

Fig. 16 shows the scatter plots for the comparison of the proposed model or the API model and the numerical experiments, together with the corresponding validation metric boundary. It is noticed that the values of validation metrics by the proposed model equal to 1 for all the six soil profiles since all the points are within the validation metric boundary, which means the proposed model shows reasonable agreement with 3D FE analyses. By contrast, the values of validation metrics by the API model equal to 1 for the case of Case SCS only, which means the API model cannot work well for monopiles. This may come from two sources: firstly, the rotational soil reactions (the coupling between axial and lateral soil resistances) are not considered in the API model; secondly, different formulae are used for the lateral soil reactions between the proposed model and the API model. To evaluate the possible reason, the predictions by the proposed model without the rotational soil reactions (shown as Present w/o coupling) are also added in Figs. 15 and 16. The proposed model without the rotational soil reactions works well for Case C, Case CS, Case CSC, and Case SC, but still does not work well for Case S and Case SCS. This reveals the necessity to consider the rotational soil reactions (the coupling between axial and lateral soil resistances) when predicting the monotonic responses of monopiles.

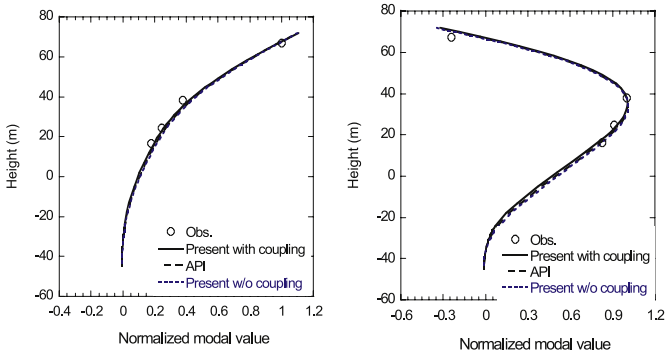

(a) Modal shape of the first mode (b) Modal shape of the second mode

Fig. 18. Comparison of measured and predicted modal shapes of first and second modes.

3.2. Effects of coupling between axial and lateral resistances on modal damping of monopile supported offshore wind turbines

As described in Kallehave et al. (2015), the modal properties of the wind turbine supporting structure are important technical levers for optimizing monopiles, which enlighten the necessity to predict the modal properties accurately. In this section, effects of coupling between axial and lateral resistances on modal damping of monopile supported offshore wind turbines are investigated by the proposed model with and without the rotational soil reactions. To quantify effects of coupling between axial and lateral resistances, an iterative procedure to determine the modal properties of an offshore wind turbine is proposed here:

Firstly, a Winkler model is built using the initial stiffness and damping coefficient of nonlinear soil reaction curves. As described in DNVGL-RP-C212 (2017), the initial stiffness for sand uses the initial slope of the p-y curve in sand while that for clay adopts the secant stiffness corresponding to the relative displacement $y/y_c = 0.1$ with the ordinate value $p/p_u = 0.23$. According to DNVGL-RP-C212 (2017) and Ishihara and Wang (2019), the initial damping coefficient can be determined using Eq. (13) with the small-strain damping only, which means that no hysteretic damping is involved at the initial state.

Secondly, a 10-min transient simulation is conducted for the operating wind turbine structure in the aeroelastic code (e.g. Bladed (Bossanyi, 2010)) with the Winkler model in the first step, in which a wind speed level equal to the targeted value is used to determine the deformation of each soil reaction.

Thirdly, the stiffness and damping coefficient in the Winkler model are updated using the deformations calculated in the second step. There are two ways to achieve this. One is described in Ishihara and Wang (2019), which converts the deformation into strain (e.g., $\gamma = (1 + \nu)y/2.5D$, γ, y, υ and D are the strain, deformation, Poisson ratio of soil and pile diameter, respectively and uses the nonlinear soil model (e.g. Hardin-Drnevich model in the JSCE guideline (Ishihara, 2010)) to determine K_{el} and β_{el}. Note that since both the small-strain damping and the hysteretic damping are incorporated in the Hardin-Drnevich model in the JSCE guideline (Ishihara, 2010), β_{el} can be directly obtained. The other way applies the hysteresis loop to determine K_{el} and β_h as illustrated in Fig. 2. Based on β_h, the damping coefficient c_{el} can be determined using Eq. (13). How to determine the damping coefficient from the hysteresis loop is described in Damgaard et al. (2013), in which, however, the contribution of the small-strain damping is not considered.

Finally, repeat the second and third steps until the convergence criteria of the modal damping ratios are met, i.e., the relative errors are less than 5% as given in Ishihara and Wang (2019).

$$c_{\mathrm{el}} = 2\beta_{\mathrm{el}}\frac{K_{\mathrm{el}}}{2\pi f};\ \beta_{\mathrm{el}} = \beta_s + \beta_h \tag{13}$$

where c_{el} is the damping coefficient, β_{el} is the foundation material damping, β_s represents the small-strain damping (e.g. 2% in JSCE guideline (Ishihara, 2010)) and β_h represents the hysteretic damping, K_{el} is the equivalent spring stiffness, f is the frequency of the first mode.

The field measurements of the Vestas 3 MW wind turbine described in Shirzadeh et al. (2013) and Shirzadeh et al. (2015) are employed in

this study to demonstrate the three-dimensional effects. Fig. 17 depicts the outline of the wind turbine and the supporting soil profile. The wind turbine information is presented in Table 6 while the soil properties are summarized in Table 7. The Poisson ratios, relative density D_r, over-consolidation ratio OCR and plasticity index I_p are estimated, based on the initial shear modulus which can be calculated following DNVGL-RP-C212 (2017). An aeroelastic model of the wind turbine is built using the aero-elastic code GH Bladed 4.8 (Bossanyi, 2010), which includes the blade aerodynamic properties, the properties of the rotor and nacelle assembly, tower, and monopile, and the hydrodynamic properties as well as the soil-structure interaction. The distributed properties of the blades are built by scaling down the data from the NREL 5 MW reference wind turbine (Jonkman et al., 2009). This can result in a small deviation on the frequencies of the blade modes but have little influence on the frequency of fundamental tower modes. The overall mass, first mass moment of inertia, second mass moment of inertia, and nominal radial CM (center of mass) location of each blade are 8244 kg, 1.3×10^5 kgm, 3.3×10^6 kgm^2, and 15.9 m with respect to the blade root, respectively. The same method has been used in Shirzadeh et al. (2013). The structural damping is modeled using the Rayleigh damping model and the structural damping ratio of the first mode is 0.2%, which is determined according to the filed measurement of a 2.4 MW wind turbine in Oh and Ishihara (2018). The structural damping ratio of the second mode adopts the same value as that of the first mode as recommended by IEC61400-6 (IEC61400-6, 2020). The monopile is modeled with 0.5 m intervals for 0∼-5 m below mudline, with 1.0 m intervals for -5∼-10 m, and with 2.0 m intervals for -10 m ∼ -26 m. A small interval is used at shallow depths because the soil-structure interactions at shallow depths are more important here.

The modal frequencies and modal shapes are obtained using the eigenvalue analysis while the modal damping ratios are estimated by performing the free decay analyses of a parked wind turbine. The first and second modes of the wind turbine supporting structure can be excited using a sinusoidal wave with the frequency same as the measured value. The simulation time is 60 s and the sinusoidal wave only lasts in the first 20 s. The wind turbine supporting structure then vibrate freely in the last 40 s and the modal damping is estimated by using these data. To eliminate the aerodynamic effect, the pitch angle and the wind speed are set as 90° and 0 m/s, respectively. Other environmental conditions such as waves, currents, and tides are turned off to eliminate the hydrodynamic effect. The effect of added mass is incorporated by introducing an added mass $m_w = 2\rho_w \frac{\pi D^2}{4} h$ (h is the water depth, see Newman (1977)). The predicted modal damping ratios, modal frequencies and modal shapes are portrayed in Table 8 and Fig. 20.

It is observed that the predictions by the proposed model match well with the measurements in terms of the modal damping ratios, the modal frequencies, and the modal shapes for both modes. However, without considering the effects of pile diameter and aspect ratio, the API model significantly underestimates the modal damping ratios. This is because the rotational soil reactions in the proposed model contribute significantly to the modal damping ratio as explained in Ishihara and Wang (2019). To show the evidence about the statements above, the predictions by the proposed model without rotational soil reactions (coupling between the axial and lateral resistances) are also added in Table 8 and Fig. 18. Compared to the API model, the predicted modal damping ratio for the first mode by the proposed model without coupling between axial and lateral resistances increases by 21.2%, but still 16.5% smaller than the field measurement. This reveals the necessity to consider coupling between the axial and lateral resistances when predicting the modal damping ratios. Generally, the lateral soil reactions on the pile shaft and base contribute to 70–80% of the monotonic responses of monopiles and the modal damping ratios for the monopile supported wind turbine while the rotational soil reactions on the pile shaft and base contribute to 20–30%. Unlike the modal damping, the modal shapes are not sensitive to the models.

Considering the wide application of the API model, many researches exist to modify the API model for the design of monopiles. The ideas can be categorized into two types. One type is to modify the soil properties (e.g. S-wave velocity by Ishihara and Wang (2019)) while the other type is to modify the initial stiffness coefficient to consider the large diameter effect (e.g. Sørensen, 2012; Kallehave et al., 2012). Obvious drawbacks exist in the two ideas. The first idea cannot reflect the mechanism of three-dimensional effects and heavily relies on the experimental data while the second idea mixes the three-dimensional effects from the large pile diameter and the small pile aspect ratio. In fact, a proper modification of the API model shall be like the proposed model in this study.

4. Conclusion

A semi-analytical 1D model is derived from the fishbone frame model for pile foundations of offshore wind turbines, which contains only one parameter identified by experiments and 3D FE analyses. The proposed model can be used for the analyses of monopile under the lateral loading without the tuning of parameters. Conclusions are summarized as:

1. A semi-analytical 1D model with the eight types of soil reactions is derived from the fishbone frame model, in which the effects of the pile diameter and aspect ratio are captured by the lateral and rotational soil reactions. The coupling between axial and lateral resistances that matters for large pile diameters and small pile aspect ratios is modeled as the rotational soil reactions. In the proposed model, the formulae of the soil reactions are analytically derived, and the parameters are identified using experiments and 3D FE analyses.
2. The correction factor for the calculation of the ultimate bearing capacities of the lateral and rotational soil reactions on the pile shaft is identified using a curve-fitting approach and validated using a series of experiments and 3D FE analyses for both sand and clay. The proposed model shows favorable agreements with experiments and 3D FE analyses in terms of the load-displacement curves at the ground level and the rotation and moment responses for the pile foundations with various pile diameters and pile aspect ratios.
3. The proposed model is further verified by monopiles in layered soils and applied to investigate the effect of coupling between axial and lateral resistances on the modal damping of a monopile supported wind turbine in layered soils. The proposed model shows good agreements with the 3D FE analyses of monopiles in layered soils and the field measurement of modal damping of the wind turbine. Without considering coupling between axial and lateral resistances, the modal damping ratios for the monopile supported wind turbine are underestimated significantly.

Declaration of competing interest

The authors declare that they have no known competing financial interests or personal relationships that could have appeared to influence the work reported in this paper.

Acknowledgement

This research was carried out as a part of the joint program funded by Shimizu Corporation, J-POWER, Toshiba Energy Systems & Solutions Corporation, MHI Vestas Offshore Wind Japan and ClassNK. The authors express their deepest gratitude to the concerned parties for their assistance during this study.

Appendix A. Constitutive relationships and input parameters for the soil reactions in the proposed model

The constitutive relationships of the soil reactions in the proposed model are demonstrated using PySimple1. PySimple1 consists of elastic ($p-y_e$), plastic ($p-y_p$), and gap ($p-y_g$) components in series, in which the gap component consists of a drag element (p^d-y^g) in parallel with a closure element (p^c-y^g). The governing equations of PySimple1 are shown in Eq. (A1)-(A10). The force and stiffness in the elastic component (Eq. (A1)-(A2)), in the plastic component (Eq. (A3)-(A4)), in the gap component (Eq. (A5)-(A8)) and in the overall spring (Eq. (A9)-(A10)) are presented herein briefly. Note that these equations depict the constitutive relationships of PySimple1 with commonly used notations, which are changed accordingly when it is applied to the p_y-v_y spring, such as p_{ult} for $p_{ult}(z)$ and y_{50} for $y_{50}(z)$. The governing equations of the $M_x-\theta_x$ spring, the $S_{y,\,\mathrm{pb}}-v_{y,\mathrm{pb}}$ spring, the $M_{x,\,\mathrm{pb}}-\theta_{x,\,\mathrm{pb}}$ spring, the t_z-v_z spring, the $Q_{z,\,\mathrm{pb}}-v_{z,\,\mathrm{pb}}$ spring, the $T_z-\varphi_z$ spring and the $T_{z,\mathrm{pb}}-\varphi_{z,\mathrm{pb}}$ spring are omitted here. For the $M_{x,\,\mathrm{pb}}-\theta_{x,\,\mathrm{pb}}$ spring, the gap component in QzSimple2 is not included.

$$p^e = K^e y^e \tag{A1}$$

$$K^e = \eta\frac{p_{ult}}{y_{50}} \tag{A2}$$

$$p^p = p_{ult} - (p_{ult}-p_0)\left(\frac{c\cdot y_{50}}{c\cdot y_{50}+|y^p-y_0^p|}\right)^n \tag{A3}$$

$$K^p = \frac{\partial p^p}{\partial y^p} = \frac{n\cdot sign(\dot{y})(p_{ult}-p_0)}{|y^p-y_0^p|+c\cdot y_{50}}\left[\left(\frac{c\cdot y_{50}}{|y^p-y_0^p|+\cdot c\cdot y_{50}}\right)^n\right] \tag{A4}$$

$$p^g = p^d + p^c \tag{A5}$$

$$p^d = C_d\cdot p_{ult} - \left(C_d\cdot p_{ult}-p_0^d\right)\left(\frac{y_{50}}{y_{50}+2|y^g-y_0^g|}\right) \tag{A6}$$

$$p^c = 1.8\cdot p_{ult}\left[\frac{y_{50}}{y_{50}+50(y_0^+-y^g)}-\frac{y_{50}}{y_{50}+50(y_0^--y^g)}\right] \tag{A7}$$

$$K^g = \frac{\partial p^g}{\partial y^g} = \frac{2n\left(p_0^d-C_d p_{ult}\right)}{y_{50}+2|y^g-y_0^g|}\left(\frac{y_{50}}{y_{50}+2|y^g-y_0^g|}\right)+\frac{1.8p_{ult}\frac{y_{50}}{50}}{\left(\frac{y_{50}}{50}-y^g+y_0^+\right)^2}-\frac{1.8p_{ult}\frac{y_{50}}{50}}{\left(\frac{y_{50}}{50}-y^g+y_0^-\right)^2} \tag{A8}$$

$$p = p^e = p^p = p^g \tag{A9}$$

$$K = \left(1/K^e+1/K^p+1/K^g\right)^{-1} \tag{A10}$$

where K^e is the elastic modulus, K^p is the plastic modulus, K^g is the gap modulus and K is the combined modulus; p_0 is the value of p at the start of current plastic loading cycle and p_{ult} is the ultimate bearing capacity; y^e is the elastic component of displacement, y^p is the plastic component of displacement, y_0^p is the value of y_0 at the start of current plastic loading cycle and y_{50} is the displacement where $p=0.5p_{ult}$. p^d and p^c are the forces in the drag element and the closure element, respectively, p_0^d is the value of p^d at the start of current plastic loading cycle; y^g is the displacement across the gap element, y_0^g is the value of y^g at the start of current plastic loading cycle and C_d is the material constant, which means the ratio of the maximum drag force to the ultimate bearing capacity. y_0^+ is the memory term for the positive side of the gap, y_0^- is the memory term for the negative side of the gap. The initial values of y_0^+ and y_0^- are $y_{50}/100$ and $-y_{50}/100$, respectively. Material constants c, n, and η define the shape of the backbone curve of the PySimple1.

The calculations of input parameters of each soil reaction curve include the ultimate bearing capacity and a representative displacement (the displacement corresponding to a half of the ultimate bearing capacity) are summarized here. Assuming that the contact between the monopile and the soil is not maintained on the backside of the monopile at a specific depth and $\sigma_r=\sigma_{r0}\cos\alpha$, $\tau_{r\alpha}=\tau_{r1}\sin\alpha$, $\tau_{rz}=\tau_{r1}\cos\alpha$, $\tau_{z\alpha}=\tau_{r2}\sin\alpha$ as well as $\tau_{zr}=\tau_{r2}\cos\alpha$, the ultimate bearing capacities $p_{ult}(z)$, $M_{ult}(z)$, $S_{ult,\mathrm{pb}}$, $M_{ult,\mathrm{pb}}$, $t_{ult}(z)$, $Q_{ult,\mathrm{pb}}$, $T_{ult}(z)$ and $T_{ult,\mathrm{pb}}$ can be calculated based on Eq. (A11)-(A18). The same assumptions were used in the development of the Winkler model of caisson foundations in Gerolymos and Gazetas (2006). The expressions of $p_{ult}(z)$, $M_{ult}(z)$, $S_{ult,\mathrm{pb}}$ and $M_{ult,\mathrm{pb}}$ can be found in Gerolymos and Gazetas (2006) while those of $t_{ult}(z)$, $Q_{ult,\mathrm{pb}}$, $T_{ult}(z)$ and $T_{ult,\mathrm{pb}}$ can be seen in Li (2017).

$$p_{ult}(z) = \left(\frac{\pi}{4}+\frac{1}{3}\tan\delta\right)D\sigma_{r0}+\frac{\pi}{4}cD \tag{A11}$$

$$M_{ult}(z) = \frac{1}{2}cD^2+\frac{\pi}{8}D^2\tan\delta\sigma_{r0} \tag{A12}$$

$$S_{ult,\mathrm{pb}} = \left(c\frac{\pi}{4}D^2+N_{\mathrm{pb}}\tan\delta\right) \tag{A13}$$

$$M_{ult,\mathrm{pb}} = \frac{1}{2}\cdot N_{\mathrm{pb}}\left(1-\frac{N_{\mathrm{pb}}}{Q_{ult,\mathrm{pb}}}\right)B \tag{A14}$$

$$t_{ult}(z) = (k_0\gamma' z\tan\delta+k_1 c)\pi D \tag{A15}$$

$$Q_{ult,\mathrm{pb}} = \eta A\left(cN_cF_{cs}F_{cd}F_{ci}+\gamma' LN_qF_{qs}F_{qd}F_{qi}+0.5\gamma' BN_\gamma F_{\gamma s}F_{\gamma d}F_{ri}\right) \tag{A16}$$

$$T_{ult}(z) = (\beta\gamma' z + \alpha c)\pi D \tag{A17}$$

$$T_{ult,\mathrm{pb}} = \frac{1}{3} D N_{\mathrm{pb}} \tan\delta + \frac{\pi}{12} D^3 \alpha c \tag{A18}$$

Here, $K_p = \tan^2\left(45^\circ + \frac{\varphi}{2}\right)$, $\tau_{r1} = c + \sigma_r \tan\delta$, $\tau_{r2} = c + \sigma_z \tan\delta$, $\delta = \left(\frac{1}{3} \sim \frac{2}{3}\right)\varphi$, $\sigma_z = \gamma' z$, $N_{\mathrm{pb}} = N_0 - \min\left(\frac{\sum_{z=0}^{L} K_{t_z}}{\sum_{z=0}^{L} K_{t_z} + K_{Q_{z,\mathrm{pb}}}} N_0,\ \sum_{z=0}^{L} t_{ult}(z)\right)$, $K_{t_z} = \left(\frac{6.8}{\pi}\left(\frac{L}{D}\right)^{-1.71} E_s\right)\pi D$, $K_{Q_{z,\mathrm{pb}}} = \frac{2G_s D}{(1-\upsilon_s)}$, $k_0 = 0.4$, $k_1 = 0.5$, $A = \frac{\pi}{4}D^2$, $B = \sqrt{A}$, $\beta = \begin{cases} 1.5 - 0.245\sqrt{z},\ 0.25 \le \beta \le 1.2 & \text{for } N_{60} \ge 15 \\ \frac{N_{60}}{15}(1.5 - 0.245\sqrt{z}) & \text{for } N_{60} < 15 \end{cases}$,

$N_{60} = [60 + 25\log(d_{50})]\cdot {D_r}^2$, $\alpha = \begin{cases} 0.55 & \text{for } \frac{c}{P_a} \le 1.5 \\ 0.55 - 0.1\left(\frac{c}{P_a} - 1.5\right) & \text{for } 1.5 \le \frac{c}{P_a} \le 2.5 \\ 0.45 & \text{for } \frac{c}{P_a} > 2.5 \end{cases}$ where c is cohesion of soil, γ' is the effective unit weight of soil, φ is the friction angle of soil, d_{50} is median particle diameter, taken as 0.37 if it is not given, D_r is the relative density of soil, P_a is the atmospheric pressure. N_c, N_q and N_γ are the bearing capacity factors, F_{cs}, F_{qs} and $F_{\gamma s}$ are the shape factors, F_{cd}, F_{qd} and $F_{\gamma d}$ are the depth factors, F_{ci}, F_{qi} and F_{ri} are the inclination factors, which can be found in Meyerhof (1963). η is the plugging coefficient. In the Chinese method (Chinese Department of Construction, 2008), $\eta = 1$ for closed-ended piles, $\eta = 0.16z/D$ when $z/D < 5$, and $\eta = 0.8$ when $z/D \ge 5$. In the FinnRA method (FinnRA, 2000), $\eta = 0.8$ for sandy soil if $z/D = 15$, and the value decreases linearly with the z/D ratio.

Once the ultimate bearing capacity of each soil spring has been obtained, the displacement corresponding to a half of the ultimate bearing capacity can be calculated using Eq. (A19)-(A26). This follows the method used in Raychowdhury and Hutchinson (2009).

$$y_{50}(z) = \eta_{p_y}\frac{p_{ult}(z)}{K_{p_y}} \tag{A19}$$

$$\theta_{50}(z) = \eta_{M_x}\frac{M_{ult}(z)}{K_{M_x}} \tag{A20}$$

$$y_{50,\mathrm{pb}} = \eta_{S_{y,\mathrm{pb}}}\frac{S_{ult,\mathrm{pb}}}{K_{S_{y,\mathrm{pb}}}} \tag{A21}$$

$$\theta_{50,\mathrm{pb}} = \eta_{M_{x,\mathrm{pb}}}\frac{M_{ult,\mathrm{pb}}}{K_{M_{x,\mathrm{pb}}}} \tag{A22}$$

$$z_{50}(z) = \eta_{t_z}\frac{t_{ult}(z)}{K_{t_z}} \tag{A23}$$

$$z_{50,\mathrm{pb}} = \eta_{Q_{z,\mathrm{pb}}}\frac{Q_{ult,\mathrm{pb}}}{K_{Q_{z,\mathrm{pb}}}} \tag{A24}$$

$$\varphi_{50}(z) = \eta_{T_z}\frac{T_{ult}(z)}{K_{T_z}} \tag{A25}$$

$$\varphi_{50,\mathrm{pb}} = \eta_{T_{z,\mathrm{pb}}}\frac{T_{ult,\mathrm{pb}}(z)}{K_{T_{z,\mathrm{pb}}}} \tag{A26}$$

Here, $K_{p_y} = \frac{0.65E_s}{1-\nu_s^2}\sqrt[12]{\frac{E_s D^4}{E_p I_p}}$, $K_{M_x} = 0.85\left(\frac{L}{D}\right)^{-1.71} E_s L^2$, $E_s = 2(1+\upsilon_s)G_s$, $I_p = \frac{\pi}{64}[D^4 - (D-2t)^4]$, $K_{S_{y,\mathrm{pb}}} = \frac{4G_s D}{(2-\upsilon_s)}$, $K_{M_{x,\mathrm{pb}}} = \frac{G_s D^3}{3(1-\upsilon_s)}$, $K_{T_z} = \frac{4G_s}{D}$, $K_{T_{z,\mathrm{pb}}} = \frac{2G_s D^3}{3(1-\upsilon_s)}$, $\eta_{p_y} = \begin{cases} 0.542 & \text{for sand} \\ 1.0204 & \text{for clay} \end{cases}$, $\eta_{M_x} = \eta_{t_z} = \eta_{S_{y,\mathrm{pb}}} = \eta_{T_z} = \eta_{T_{z,\mathrm{pb}}} = \begin{cases} 2.05 & \text{for sand} \\ 0.708 & \text{for clay} \end{cases}$, $\eta_{Q_{z,\mathrm{pb}}} = \eta_{M_{x,\mathrm{pb}}} = \begin{cases} 1.39 & \text{for sand} \\ 0.525 & \text{for clay} \end{cases}$

where G_s and υ_s are the shear modulus and Poisson ratio of soil, respectively. t and E_p are the thickness and Young's modulus of monopile, respectively. K_{p_y}, K_{M_x}, $K_{S_{y,\mathrm{pb}}}$ and $K_{M_{x,\mathrm{pb}}}$ can be found in Gerolymos and Gazetas (2006), while K_{t_z}, $K_{Q_{z,\mathrm{pb}}}$, K_{T_z} and $K_{T_{z,\mathrm{pb}}}$ can be seen in Li (2017). η_{p_y}, η_{t_z} and $\eta_{Q_{z,\mathrm{pb}}}$ can be found in McKenna (2011).

Appendix B. Description of 3D FE analyses in OpenSees

The computer program OpenSees (McKenna, 2011) is used for the pushover analyses. The nonlinear inelastic stress-strain response of the soil is simulated using the Pressure Dependent Multi Yield (PDMY) constitutive model for sand and the Pressure Independent Multi Yield (PIMY) constitutive model for clay as available in OpenSees (Yang et al., 2008). The input parameters for the two models are presented in Table B1. Following Corciulo et al. (2017), the interface layer is as thick as 4% of the pile diameter and is assumed to behave as the neighboring soil material with a reduced friction angle or undrained shear strength. Soil elements at a distance greater than 8D (D: pile diameter) from the pile are coarser, while the elements at a

distance less than 8D from the pile are finer.

Fig. B1 demonstrates the finite element mesh of Case DM3, which is halved along the direction of loading due to the symmetry of the model along the axis y. The pile stiffness, the cross-sectional area of the pile, and the applied static loads are halved. At each elevation, the pile nodes are horizontally connected to the soil nodes using 7 rigid beam-column elements. The finite element mesh contains 9800 elements to represent a soil domain with a length of 26.8 m (35D) and a width of 13.4 m (17.5D) and a depth of 30.0 m (39D), which is large enough to minimize the effects of boundaries on the response of the pile. The nodes located at the base of the mesh are fixed in all directions. The nodes at equal depths on the lateral boundaries are constrained to have equal displacements. The nodes on the plane which halves the model constrained along the axis y. The FE matrix equation is integrated in time using a single-step predictor multi-corrector scheme of the static load control type with the load factor increment of 1. The solution is obtained using the modified Newton-Raphson approach with Krylov subspace acceleration. On this basis, the initial tangent stiffness of the system (after application of gravity) is used for all steps and iterations to achieve the prescribed tolerance (the normalized displacement increment less than 10^{-4}). Penalty constraints were used to enforce the prescribed displacement boundary conditions. The numbering of nodal degrees of freedom was performed using a reverse Cuthill–McKee algorithm.

Table B1
Parameters of PDMY and PIMY for simulating the soil behavior

Parameter	PISA sand	PISA clay
G_r (MPa)	See Fig. 3a	See Fig. 3b
B_r (MPa)	$B_r = \frac{2G_r(1+\nu)}{3(1-2\upsilon)}$	$B_r = \frac{2G_r(1+\nu)}{3(1-2\upsilon)}$
c_u (kPa)	0.0	See Fig. 3c
φ (deg)	40	0.0
γ_{max}	0.1	0.1
φ_{PT} (deg)	27	–
n	0.5	–
$d1$	0.8	–
$d2$	5	–
c	0.03	–

Note: G_r, low-strain shear modulus; B_r, low-strain bulk modulus; ν, Poisson ratio; c_u, undrained shear strength; γ_{max}, octahedral shear strain at which the maximum shear strength is reached; n, a constant defining variation of shear modulus as a function of mean effective confinement; φ, soil friction angle; φ_{PT}, phase transformation angle; $d1$ and $d2$, dilation parameters; c, contraction parameter.

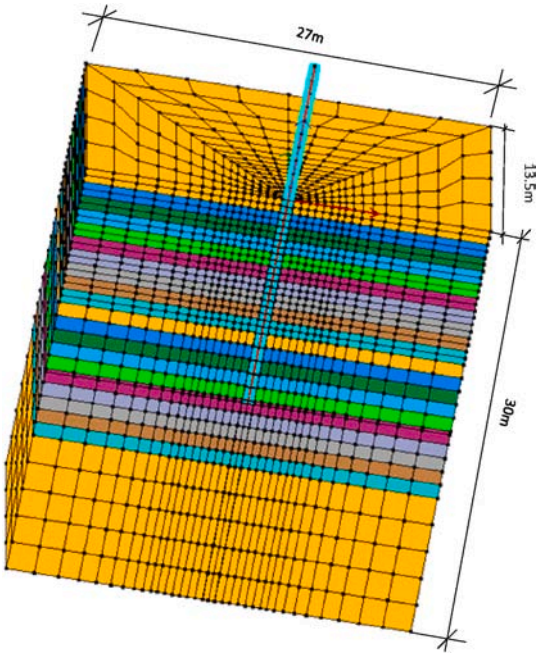

Fig. B1. The finite element mesh of Case DM3 (visualized by OpenSeesPL (Lu et al., 2011))

References

Achmus, M., Terceros, M., Thieken, K., 2016. Evaluation of p-y approaches for large diameter monopiles in soft clay. In: The 26th International Ocean and Polar Engineering Conference. OnePetro.

Andresen, L., Jostad, H.P., 1999. Application of an anisotropic hardening model for undrained response of saturated clay. In: In Numerical Models in Geomechanics. CRC Press, pp. 581–585.

API RP 2A-WSD, 2010. Recommended Practice for Planning, Designing and Constructing Fixed Offshore Platforms. American Petroleum Institute.

API RP 2GEO, 2014. Geotechnical and Foundation Design Considerations. American Petroleum Institute.

Ashour, M., Helal, A., 2014. Contribution of vertical skin friction to the lateral resistance of large-diameter shafts. J. Bridge Eng. 19 (2), 289–302.

Benz, T., 2007. Small-strain Stiffness of Soils and its Numerical Consequences. Univ. Stuttgart, Inst. f. Geotechnik., Stuttgart, Germany. PhD thesis.

Beuckelaers, W., 2017. Numerical Modelling of laterally Loaded Piles for Offshore Wind Turbines. University of Oxford PhD thesis.

Bossanyi, E.A., 2010. Bladed Theory Manual: Version 4.1. GH & Partners Ltd, 2, pp. 56–58.

Boulanger, R.W., 2000. The PySimple1 Material, Document for the OpenSees Platform. http://opensees.berkeley.edu.

Boulanger, R.W., Curras, C.J., Kutter, B.L., Wilson, D.W., Abghari, A., 2002. Seismic soil-pile-structure interaction experiments and analyses. J. Geotech. Geoenviron. Eng. 125 (9), 750–759.

Burd, H.J., Taborda, D.M.G., Zdravkovic, L., Abadie, C.N., Byrne, B.W., Houlsby, G.T., et al., 2020. PISA design model for monopiles for offshore wind turbines: application to a marine sand. Geotechnique 70 (11), 1048–1066.

Byrne, B.W., Burd, H.J., Zdravkovic, L., Abadie, C.N., Houlsby, G.T., Jardine, R.J., et al., 2019a. PISA design methods for offshore wind turbine monopiles. Proc. Annu. Offshore Technol. Conf.

Byrne, B.W., McAdam, R.A., Burd, H.J., Beuckelaers, W.J.A.P., Gavin, K., Houlsby, G.T., et al., 2019b. Monotonic laterally loaded pile testing in a stiff glacial clay till at Cowden. Geotechnique 70 (11), 970–985.

Byrne, B.W., Houlsby, G.T., Burd, H.J., Gavin, K.G., Igoe, D.J.P., Jardine, R.J., et al., 2020. PISA design model for monopiles for offshore wind turbines: application to a stiff glacial clay till. Geotechnique 70 (11), 1030–1047.

Chandler, R., 2009. The in-situ measurement of the undrained shear strength of clays using the field vane. ASTM International, West Conshohocken, PA, USA, pp. 13–44.

Chanmee, N., Chai, J., Hino, T., Wang, J., 2017. Methods for evaluating overconsolidation ratio from piezocone sounding results. Undergr. Space 2 (3), 182–194.

Chinese Department of Construction, 2008. JGJ 94-2008: Technical code for building pile foundations (In Chinese).

Corciulo, S., Zanoli, O., Pisanò, F., 2017. Transient response of offshore wind turbines on monopiles in sand: role of cyclic hydro–mechanical soil behaviour. Comput. Geotech. 83, 221–238.

Damgaard, M., Ibsen, L.B., Andersen, L.V., Andersen, J.K.F., 2013. Cross-wind modal properties of offshore wind turbines identified by full scale testing. J. Wind Eng. Ind. Aerod. 116, 94–108.

DNVGL-ST-0126, 2016. Support Structures for Wind Turbines. DNV, Oslo, Norway.

DNVGL-RP-C212, 2017. Offshore Soil Mechanics and Geotechnical Engineering. DNV, Oslo, Norway.

FinnRA, 2000. Steel Pipe Piles, Helsinki.

Fu, D., Zhang, Y., Aamodt, K.K., Yan, Y., 2020. A multi-spring model for monopile analysis in soft clays. Mar. Struct. 72, 102768.

Gerolymos, N., Gazetas, G., 2006. Development of Winkler model for static and dynamic response of caisson foundations with soil and interface nonlinearities. Soil Dynam. Earthq. Eng. 26 (5), 363–376.

He, R., Kaynia, A.M., Zhang, J., 2019a. A poroelastic solution for dynamics of laterally loaded offshore monopiles. Ocean Eng. 178, 337–350.

He, R., Kaynia, A.M., Zhang, J., Chen, W., Guo, Z., 2019b. Influence of vertical shear stresses due to pile-soil interaction on lateral dynamic responses for offshore monopiles. Mar. Struct. 64, 341–359.

He, R., Kaynia, A.M., Zhu, T., 2021. Effect of base shear and moment on lateral dynamic behavior of monopiles. Ocean Eng. 228, 108957.

IEC61400-6, 2020. Wind energy generation systems – Part 6: Tower and foundation design requirements. International Electrotechnical Commission.

Ishihara, T. (Ed.), 2010. Guidelines for Design of Wind Turbine Support Structures and Foundations (In Japanese).

Ishihara, T., Wang, L., 2019. A Study of Modal Damping for Offshore Wind Turbines Considering Soil Properties and Foundation Types. Wind Energy 22 (12), 1760–1778.

Jonkman, J., Butterfield, S., Musial, W., Scott, G., 2009. Definition of a 5-MW reference wind turbine for offshore system development. National Renewable Energy Laboratory, Golden. CO. Technical Report No. NREL/TP-500-38060.

Kallehave, D., Thilsted, C.L.B., Liingaard, M.A., 2012. Modification of the API P-Y Formulation of Initial Stiffness of Sand. In Offshore site investigation and geotechnics: integrated technologies-present and future, OnePetro.

Kallehave, D., Byrne, B.W., LeBlanc Thilsted, C., Mikkelsen, K.K., 2015. Optimization of monopiles for offshore wind turbines. Philos. Trans. R. Soc. Math. Phys. Eng. Sci. 373 (2035), 20140100.

Khaloo, A.R., Khosravi, H., 2013. Modified fish-bone model: a simplified MDOF model for simulation of seismic responses of moment resisting frames. Soil Dynam. Earthq. Eng. 55, 195–210.

Ladd, C.C., DeGroot, D.J., 2004. Recommended practice for soft ground site characterization : Arthur casagrande Lecture. In: Massachusetts Institute of Technology.

Ladd, C.C., Foott, R., 1974. New design procedure for stability of soft clays. ASCE J Geotech Eng Div 100 (7), 763–786.

Li, Q., 2017. Investigation of Drilled Shafts under Axial, Lateral, and Torsional Loading. Oregon State University PhD thesis.

Lim, H., Jeong, S., 2018. Simplified p-y curves under dynamic loading in dry sand. Soil Dynam. Earthq. Eng. 113, 101–111.

Liu, R., Zhou, L., Lian, J., Ding, H., 2016. Behavior of monopile foundations for offshore wind farms in sand. J. Waterw. Port, Coast. Ocean Eng. 142 (1), 04015010.

Lu, J., Elgamal, A., Yang, Z., 2011. OpenSeesPL: 3D Lateral Pile-Ground Interaction User Manual (Beta 1.0). Department of Structural Engineering, University of California, San Diego.

Malekjafarian, A., Jalilvand, S., Doherty, P., Igoe, D., 2021. Foundation damping for monopile supported offshore wind turbines: a review. Mar. Struct. 77, 102937.

McAdam, R.A., Byrne, B.W., Houlsby, G.T., Beuckelaers, W.J.A.P., Burd, H.J., Gavin, K., et al., 2019. Monotonic laterally loaded pile testing in a dense marine sand at Dunkirk. Geotechnique 70 (11), 986–998.

McKenna, F., 2011. OpenSees: a framework for earthquake engineering simulation. Comput. Sci. Eng. 13 (4), 58–66.

Meyerhof, G.G., 1963. Some recent research on the bearing capacity of foundations. Can. Geotech. J. 1 (1), 16–26.

Minga, E., Burd, H.. Validation report of PLAXIS MeDeTo based on the Dunkirk sand PISA field tests. https://communities.bentley.com/products/geotechnical1/w/wiki/45422/theoretical-background-of-plaxis-modeto-the-pisa-project.

Newman, J.N., 1977. The motions of a floating slender torus. J. Fluid Mech. 83 (4), 721–735.

Oettl, D., 2015. Quality assurance of the prognostic, microscale wind-field model GRAL 14.8 using wind-tunnel data provided by the German VDI Guideline 3783-9. J. Wind Eng. Ind. Aerodyn. 142, 104–110.

Oh, S., Ishihara, T., 2018. Structural parameter identification of a 2.4 MW bottom fixed wind turbine by excitation test using active mass damper. Wind Energy 21 (11), 1232–1238.

Panagoulias, S., Hosseini, S., 2018. An Innovative Design Methodology for Offshore Wind Monopile Foundations. In Proc. 26th European Young Geotechnical Engineers Conference, Graz, Austria.

Panagoulias, S., Hosseini, S., Brinkgreve, R., Burd, H.J., 2019. Design of laterally-loaded monopiles in layered soils. In: Proc. 2nd Int. Conf. Nat. Hazards & Infrastruct. National Technical University of Athens.

Plaxis, 2019. Plaxis 3D Reference Manual. Technology.

Randolph, M.F., 1981. Piles subjected to torsion. J. Geotech. Eng. Div. 107 (8), 1095–1111.

Raychowdhury, P., Hutchinson, T.C., 2009. Performance evaluation of a nonlinear Winkler-based shallow foundation model using centrifuge test results. Earthq. Eng. Struct. Dynam. 38 (5), 679–698.

Reese, L.C., Cox, W.R., Koop, F.D., 1974. Analysis of laterally loaded piles in sand. Proc. Annu. Offshore Technol. Conf.

Schatzmann, M., Olesen, H.F.J., 2010. COST 732 model evaluation case studies: approach and results. COST Off Brussels 121.

Shadlou, M., Bhattacharya, S., 2016. Dynamic stiffness of monopiles supporting offshore wind turbine generators. Soil Dynam. Earthq. Eng. 88, 15–32.

Shirzadeh, R., Devriendt, C., Bidakhvidi, M.A., Guillaume, P., 2013. Experimental and computational damping estimation of an offshore wind turbine on a monopile foundation. J. Wind Eng. Ind. Aerod. 120, 96–106.

Shirzadeh, R., Weijtjens, W., Guillaume, P., Devriendt, C., 2015. The dynamics of an offshore wind turbine in parked conditions: a comparison between simulations and measurements. Wind Energy 18(10), 1685–1702.

Sørensen, S.P.H., 2012. Soil-structure interaction for nonslender, large-diameter offshore monopiles. Aalborg University PhD thesis.

Sørensen, S.P.H., Ibsen, L.B., Augustesen, A.H., 2010. Effects of diameter on initial stiffness of p-y curves for large-diameter piles in sand. In: Numerical Methods in Geotechnical Engineering, pp. 907–912.

Taborda, D.M.G., Zdravković, L., Potts, D.M., Burd, H.J., Byrne, B.W., Gavin, K., et al., 2019. Finite element modelling of laterally loaded piles in a dense marine sand at Dunkirk. Geotechnique 70 (11), 1014–1029.

Taghavi, A., McVay, M., Niraula, L., Davidson, M., Patil, A., 2020. Axial and lateral resistance coupling in the analysis of large-diameter drilled shafts. Eng. Struct. 206, 110160.

Thieken, K., Achmus, M., Lemke, K., 2015. A new static p-y approach for piles with arbitrary dimensions in sand. Geotechnik 38 (4), 267–288.

VDI, 2005. VDI Guideline 3783, Part 9, Environmental Meteorology–Prognostic Microscale Wind Field Models – Evaluation for Flow Around Buildings and

Obstacles. Commission of Air Pollution Prevention of VDI and DIN, Düsseldorf, Germany, p. 53.
Wang, X., Zeng, X., Li, J., 2018. Assessment of bearing capacity of axially loaded monopiles based on centrifuge tests. Ocean Eng. 167, 357–368.
Wang, H., Wang, L.Z., Hong, Y., He, B., Zhu, R.H., 2020a. Quantifying the influence of pile diameter on the load transfer curves of laterally loaded monopile in sand. Appl. Ocean Res. 101, 102196.
Wang, L., Lai, Y., Hong, Y., Mašín, D., 2020b. A unified lateral soil reaction model for monopiles in soft clay considering various length-to-diameter (L/D) ratios. Ocean Eng. 212, 107492.
Wiemann, J., Lesny, K., Richwien, W., 2004. Evaluation of the pile diameter effects on soil-pile stiffness. In: Proc. of 7th German Wind Energy Conference (DEWEK).
Wikipedia. https://en.wikipedia.org/wiki/Control_variates.
Xu, Z.D., Wu, Z., 2007. Energy damage detection strategy based on acceleration responses for long-span bridge structures. Eng. Struct. 29 (4), 609–617.
Yang, Z., Lu, J., Elgamal, A., 2008. In: OpenSees soil models and solid-fluid fully coupled elements user's manual, first ed. Department of Structural Engineering, University of California, San Diego.
Yang, M., Ge, B., Li, W., Zhu, B., 2016. Dimension effect on py model used for design of laterally loaded piles. Procedia Eng. 143, 598–606.
Yoo, M.T., Choi, J.I., Han, J.T., Kim, M.M., 2013. Dynamic P-Y curves for dry sand from centrifuge tests. J. Earthq. Eng. 17 (7), 1082–1102.
Zdravković, L., Jardine, R.J., Taborda, D.M.G., Abadias, D., Burd, H.J., Byrne, B.W., et al., 2019a. Ground characterisation for PISA pile testing and analysis. Geotechnique 70 (11), 945–960.
Zdravković, L., Taborda, D.M.G., Potts, D.M., Abadias, D., Burd, H.J., Byrne, B.W., et al., 2019b. Finite element modelling of laterally loaded piles in a stiff glacial clay till at Cowden. Geotechnique 70 (11), 999–1013.
Zhang, Y., Andersen, K.H., 2019. Soil reaction curves for monopiles in clay. Mar. Struct. 65, 94–113.